Chemistry-climate feedback of atmospheric methane in a methane emission flux driven chemistry-climate model

Laura Stecher[1], Franziska Winterstein[1], Patrick Jöckel[1], Michael Ponater[1], Mariano Mertens[1,2], and Martin Dameris[1]

[1]Deutsches Zentrum für Luft- und Raumfahrt, Institut für Physik der Atmosphäre, Oberpfaffenhofen, Germany
[2]Faculty of Aerospace Engineering, Section Operations and Environment, Delft University of Technology, 2629 HS, Delft, The Netherlands

Correspondence: Laura Stecher (laura.stecher@dlr.de)

Abstract.

The chemical sink of atmospheric methane (CH_4) depends on the temperature and on the chemical composition. Here, we assess the feedback on atmospheric CH_4 induced by changes of the chemical sink in a warming climate using a CH_4 emission flux driven setup of the chemistry-climate model EMAC, in which the chemical feedback of CH_4 mixing ratios can evolve explicitly. We perform idealized perturbation simulations driven either by increased carbon dioxide (CO_2) mixing ratios, or by increased CH_4 emission fluxes. The CH_4 emission flux perturbation leads to a large increase of CH_4 mixing ratios. Remarkably, the factor by which the CH_4 mixing ratio increases is larger than the increase factor of the emission flux, because the atmospheric lifetime of CH_4 is extended.

In contrast, the individual effect of the global surface air temperature (GSAT) increase is to shorten the CH_4 lifetime, which results in a significant reduction of CH_4 mixing ratios in our setup. The corresponding radiative feedback is estimated at -0.041 W m^{-2} K^{-1} and -0.089 W m^{-2} K^{-1} for the CO_2 and CH_4 perturbation, respectively. The explicit response of CH_4 mixing ratios leads to secondary feedbacks on the hydroxyl radical (OH) and ozone (O_3). Firstly, the OH response includes the CH_4-OH feedback, which enhances the CH_4 lifetime change, and, secondly, the formation of tropospheric O_3 is reduced. Our CH_4 perturbation induces the same response of GSAT per effective radiative forcing (ERF) as the CO_2 perturbation, which supports the applicability of the ERF framework for CH_4.

1 Introduction

Methane (CH_4) is, after carbon dioxide (CO_2), the second most important anthropogenic greenhouse gas (GHG). Compared to CO_2, CH_4 has a larger radiative efficiency (Forster et al., 2021) and a shorter atmospheric lifetime of about 10 years (e.g., Prather et al., 2012; Stevenson et al., 2020). Therefore, reducing atmospheric CH_4 mixing ratios is considered an important measure to mitigate climate change on a decadal time scale (Saunois et al., 2016; Collins et al., 2018; Ocko et al., 2021; Staniaszek et al., 2022). The relative short atmospheric lifetime of CH_4 is a consequence of the fact that CH_4 is a chemically active species. According to Saunois et al. (2020), the most important sink of atmospheric CH_4 is oxidation by the hydroxyl

radical (OH). Thus, understanding the chemical mechanisms underlying CH_4 oxidation is crucial when assessing its climate impact and mitigation options.

25   Besides its direct radiative effect, indirect contributions from ozone (O_3) and stratospheric water vapour (H_2O) enhance the effective radiative forcing (ERF) of CH_4 (Shindell et al., 2005, 2009; Stevenson et al., 2013; Winterstein et al., 2019; Thornhill et al., 2021b; O'Connor et al., 2022). In addition to its climate impact, tropospheric O_3 poses harmful effects on human health (Nuvolone et al., 2018) and on vegetation (Ashmore, 2005). Therefore, mitigation options involving CH_4 emission reductions have beneficial effects on air quality (Shindell et al., 2012; Staniaszek et al., 2022) and plant productivity (Sitch et al., 2007). In

30   addition to the effects on O_3 and H_2O, CH_4 oxidation reduces OH, which feeds back onto its own atmospheric lifetime (e.g., Winterstein et al., 2019) and affects the rate of formation of secondary aerosols leading to a shift in the aerosol-size distribution. The latter, in turn, influences aerosol-radiation interactions and aerosol-cloud interactions, and is considered another indirect contribution to the ERF of CH_4 (Kurtén et al., 2011; O'Connor et al., 2022).

Next to its importance for indirect contributions to the ERF, CH_4 oxidation largely constrains the atmospheric lifetime of

35   CH_4 and, thus, together with the magnitude of the emissions, its direct radiative effect. The atmospheric lifetime of CH_4 is not constant, but depends on the temperature and on the chemical background, which determines the abundance of its sink reactants, especially OH. OH is influenced by a multitude of factors (e.g., Voulgarakis et al., 2013; Stevenson et al., 2020). Among others, meteorological factors such as humidity and temperature influence the abundance of OH. Hence, climate feedbacks of the chemical sink of CH_4 and thereby its lifetime are to be expected. More precisely, the CH_4 lifetime is projected to shorten as a

40   result of tropospheric warming (Voulgarakis et al., 2013; Stecher et al., 2021; Heimann et al., 2020; Thornhill et al., 2021a). To date, only a limited number of studies have assessed the corresponding response of CH_4 mixing ratios directly (Heimann et al., 2020). Even though efforts are ongoing to employ chemistry-climate models (CCMs) in a CH_4 emission flux driven model setup (Shindell et al., 2013; He et al., 2020; Folberth et al., 2022), it is still common practice to prescribe CH_4 mixing ratios at the lower boundary. For instance, the latter method was pursued in the Aerosol Chemistry Model Intercomparison Project

45   (AerChemMIP; Collins et al., 2017), which was endorsed in the Coupled-Model Intercomparison Project 6 (CMIP6; Eyring et al., 2016), that, in turn, built the basis for the last report of the Intergovernmental Panel on Climate Change (IPCC, 2021).

When CH_4 mixing ratios are prescribed at the surface, the CH_4 adjustment to changes of the chemical sink is suppressed in the troposphere, and can be only derived offline from the atmospheric lifetime change (Dietmüller et al., 2014; Heinze et al., 2019; Thornhill et al., 2021a). This offline method, however, suppresses indirect feedbacks induced by the CH_4 response.

50   Firstly, when CH_4 mixing ratios are free to evolve, the resulting CH_4 response alters the atmospheric CH_4 lifetime, which in turn leads to further changes of the CH_4 mixing ratios. The derivation of the CH_4 response from the lifetime change usually accounts for this effect by including a constant CH_4-OH feedback factor f (Heinze et al., 2019; Thornhill et al., 2021a) so that the equilibrium CH_4 mixing ratio $[CH_4]_{eq}$ is estimated as (e.g., Stevenson et al., 2020)

$$[CH_4]_{eq} = [CH_4]_{ref}(\frac{\tau_{exp}}{\tau_{ref}})^f, \tag{1}$$

55   where $[CH_4]_{ref}$ is the reference CH_4 mixing ratio and τ_{ref} and τ_{exp} are the reference and perturbed atmospheric lifetimes of CH_4, respectively. Estimates of f are in the range of 1.19 to 1.55 (Fiore et al., 2009; Voulgarakis et al., 2013; Stevenson et al.,

2013; Thornhill et al., 2021b; Stevenson et al., 2020; Sand et al., 2023). Holmes (2018) found that f can vary geographically and seasonally, and that it strengthens with an increasing CH_4 burden. Secondly, the subsequent CH_4 response affects other chemical constituents such as O_3. This effect is also sometimes accounted for by scaling the sensitivity of O_3 towards CH_4

60   perturbations with the expected CH_4 response (Fiore et al., 2009; Thornhill et al., 2021b). However, previous studies that assessed the climate feedback of O_3 and the corresponding implication for the global surface air temperature (GSAT) response did not, or only rudimentarily, account for the interaction between changes of O_3 and CH_4 (Dietmüller et al., 2014; Nowack et al., 2015; Marsh et al., 2016; Li and Newman, 2023). As for O_3 alone the latter studies indicate that its feedback reduces the resulting GSAT response, or in other words that it is a negative feedback. The magnitude of this feedback, however, is highly

65   model dependent.

   In this study, we use a CH_4 emission flux driven setup of the CCM ECHAM/MESSy Atmospheric Chemistry (EMAC; Jöckel et al., 2016) to explicitly simulate the response of atmospheric CH_4 mixing ratios resulting from changes in the chemical sink and in CH_4 emissions. We perform idealized perturbation simulations with either increased CO_2 mixing ratios (with CO_2 being an inert GHG), or increased CH_4 emission fluxes. The CH_4 perturbation affects the chemical composition directly,

70   whereas the CO_2 perturbation influences the chemical composition only indirectly, e.g. through the temperature change. From the simulation results we assess the change in CH_4 mixing ratios and its implications for OH and O_3. In addition to the CH_4 feedback, GSAT changes induce other processes that influence O_3. For instance, temperature changes affect chemical reaction rates, emissions of precursor species from natural sources, circulation, or the abundance of H_2O (e.g., Stevenson et al., 2006; Chiodo et al., 2018; Abalos et al., 2020; Griffiths et al., 2021; Zanis et al., 2022). Therefore, we apply an attribution method for

75   O_3 (TAGGING; Grewe et al., 2017; Rieger et al., 2018) to identify and quantify the importance of individual source categories that influence tropospheric O_3 under tropospheric warming.

   Our analysis is based on the ERF conceptual framework (Shine et al., 2003; Hansen et al., 2005; Ramaswamy et al., 2018; Forster et al., 2021), which means that the so-called fast and (slow) climate responses are assessed separately. The fast response represents the part of the full response that develops, on short time scales, independent of the corresponding GSAT change,

80   whereas the climate response represents the isolated effect of the GSAT change. There is no formal time scale that separates the fast and slow responses, but they are distinguished conceptually by the dependence on the GSAT response, which is coupled to the (slow) response of the ocean. It is noteworthy that the CH_4 adjustment that follows the increase of CH_4 emission fluxes evolves on the time scale of decades, whereas typical physical (rapid) adjustments evolve on the time scale of weeks or months (e.g., Smith et al., 2018). We derive ERF and the fast response from simulations with prescribed sea surface temperatures (SSTs)

85   and sea ice concentrations (SICs) as recommended by Forster et al. (2016). The climate response is assessed as the difference between the response in a simulation coupled to a mixed layer ocean model and the respective fast response. Analogously, we assess (rapid radiative) adjustments as the radiative effects corresponding to changes in the fast response and (slow climate) feedbacks as the radiative effects corresponding to changes in the climate response.

   The paper is structured as follows. Section 2 explains the simulation set-up (Sect. 2.1.), as well as the TAGGING method to

90   attribute O_3 to individual source categories (Sect. 2.2.), and the method to derive the radiative effects corresponding to composition changes of individual species (Sect. 2.3.). Additionally, Sect. 2.3. introduces the theoretical framework for radiative

forcing and climate sensitivity. Section 3 presents the simulation results. In Sect. 3.1. and 3.2., we present composition changes in the CO_2 and CH_4 perturbation simulations, respectively. In Sect. 3.3., the corresponding radiative effects are addressed. We conclude with a general discussion and summary of our findings in Sect. 4. Parts of the paper are based on the PhD thesis of the first author (Stecher, 2024).

2 Methods

2.1 Model description and simulation strategy

We use the modular CCM ECHAM/MESSy Atmospheric Chemistry (EMAC; Jöckel et al., 2016) in version 2.55.2. All simulations are performed at a resolution of T42L90MA, i.e. at a triangular (T) truncation at wave number 42 of the spectral dynamical core, corresponding to a quadratic Gaussian grid of approximately $2.8° \times 2.8°$ resolution in latitude and longitude and 90 vertical levels, with the uppermost level centered around 0.01 hPa. The simulations are performed as time slices, which means that the same boundary conditions are repeated cyclically for each simulation year. The boundary conditions, i.e. prescribed emissions and mixing ratios of well-mixed GHGs, represent the year 2010. The quasi-biennial oscillation (QBO) is nudged following the method of Giorgetta and Bengtsson (1999) as described by Jöckel et al. (2016), which introduces some interannual variability. The simulation set-up builds on previous studies assessing the impact of enhanced CH_4 mixing ratios with EMAC (Winterstein et al., 2019; Stecher et al., 2021), with the important advance that for the present study EMAC is used in a CH_4 emission flux driven setup, which means that CH_4 emission fluxes instead of CH_4 mixing ratios are prescribed at the lower boundary. The CH_4 emission fluxes are prescribed as offline emission fluxes, i.e. there are no feedbacks on CH_4 emission fluxes from natural sources such as wetlands or permafrost, which are expected to change in a changing climate (e.g., O'Connor et al., 2010; Dean et al., 2018).

The applied CH_4 emission inventory is an inverse optimized inventory for the EMAC model (Frank, 2018). For the two reference simulations (see Tab. 1 and text below), monthly mean emissions of the year 2010 are repeated cyclically and scaled by a globally constant factor of 1.08, which corresponds to total annual mean emissions of 625.3 $Tg(CH_4)$ a^{-1}. The scaling was applied to bring the simulated CH_4 surface mixing ratios closer to observations. As the tropospheric mean CH_4 lifetime is about 10 years (e.g., Prather et al., 2012; Stevenson et al., 2020), the CH_4 mixing ratios of the year 2010 result not only from CH_4 emissions of the year 2010, but also from emissions of the years before. Therefore, it can not be expected that the cyclic repetition of CH_4 emissions of the year 2010 results in CH_4 mixing ratios that represent the year 2010 exactly. Applying the scaling, the resulting global mean CH_4 surface mixing ratio is 1.82 ppmv for both reference simulations. This is in close agreement with observational estimates for the years 2010 and 2012 of 1.80 and 1.81 ppmv by the National Oceanic and Atmospheric Administration Earth System Research Laboratories (NOAA/ESRL) (Lan et al., 2023), and 1.81 and 1.82 ppmv by the WMO World Data Centre for Greenhouse Gases (WMO, 2022). The estimates of NOAA/ESRL tend to be lower, as only unpolluted marine surface sites contribute to the global estimate. The chemical sink reactions of CH_4 with OH, excited oxygen ($O(^1D)$) and chlorine (Cl), and CH_4 photolysis are interactively accounted for by the MESSy submodels Module Efficiently Calculating the Chemistry of the Atmosphere (MECCA; Sander et al. (2019)) and JVAL (Sander et al., 2014). Oxidation by OH

125 dominates the tropospheric CH_4 sink, so that the reaction with Cl accounts for only 0.23% of the total chemical tropospheric CH_4 loss (see Tab. S1 in the supplement). Therefore, we focus on CH_4 lifetime changes with respect to oxidation by OH. In addition to the sink reactions of CH_4, the chemical mechanism covers the basic chemistry of O_3, OH, hydroperoxyl (HO_2), nitrogen oxides, alkanes and alkenes up to four C-atoms, and isoprene (C_5H_8). Further, halogen chemistry of bromine and chlorine species is included. Alkynes, aromatics and mercury are not considered. In total, the used mechanism covers 265 gas-

130 phase, 82 photolysis and 12 heterogeneous reactions of 160 species. The chemical feedback on H_2O modifies the prognostic specific humidity, and vice versa. The soil sink of CH_4 is included by the submodel DDEP (Kerkweg et al., 2006a), which uses a prescribed deposition rate (Spahni et al., 2011; Curry, 2007) that is scaled to the actual CH_4 mixing ratio in the corresponding grid box. On average, the global soil sink is 27.6 $Tg(CH_4)\,a^{-1}$ for both reference simulation.

Precursor emissions of O_3, in particular nitrogen oxides NO and NO_2 (NO_x), non-methane hydrocarbons (NMHCs), and

135 carbon monoxide (CO), are treated as described by Jöckel et al. (2016). Anthropogenic emissions of these species are prescribed from the MACCity inventory (Lamarque et al., 2010; Granier et al., 2011; Diehl et al., 2012), whereby the (mostly monthly resolved) emission fluxes of the year 2010 are repeated cyclically. In addition, climatologies of biogenic emissions of NMHCs and CO are prescribed from the Global Emissions InitiAtive (GEIA). Natural emissions of NO_x from lightning, NO_x and C_5H_8 from biogenic sources, as well as the exchange of chemical species between the atmosphere and ocean are parameterized. For

140 lightning NO_x the parameterization of Grewe et al. (2001) is used in the MESSy submodel LNOX (Tost et al., 2007). The 20-year mean global emissions from lightning NO_x are 5.2 $Tg(N)\,a^{-1}$ for both reference simulations (see Tab. 3). Interactive biogenic emissions of soil NO_x and C_5H_8 are calculated by the submodel ONEMIS (Kerkweg et al., 2006b). On average, biogenic NO_x emissions are 6 $Tg(N)\,a^{-1}$ and biogenic C_5H_8 emissions are about 307 $Tg(C)\,a^{-1}$ for both reference simulations (see Tab. 3). The atmosphere-ocean exchange of the chemical species C_5H_8, dimethyl sulfide (DMS) and methanol (CH_3OH)

145 is parameterized using the submodel AIRSEA (Pozzer et al., 2006). The mixing ratios of CO_2, nitrous oxide (N_2O) and ozone depleting substances (ODS) are prescribed at the lower boundary using monthly mean values of the year 2010 (Meinshausen et al., 2011; Carpenter et al., 2018). For the radiation, a CFC-11 equivalent is calculated lumping additional radiatively active ODS via radiative efficiencies following the approach by Meinshausen et al. (2017). For the short-lived halocarbons $CHCl_2Br$, $CHClBr_2$ and CH_2ClBr, as well as CH_2Br_2 and $CHBr_3$ surface emissions are prescribed from Warwick et al. (2006) and

150 Liang et al. (2010), respectively.

Table 1 summarizes the performed simulations. The simulations REF-SSTfix and REF-SSTvar serve as references for the experiment simulations and represent year 2010 conditions. REF-SSTfix is performed using prescribed SSTs and SICs, whereas for REF-SSTvar a mixed layer ocean (MLO) model is coupled (MESSy submodel MLOCEAN, Kunze et al. (2014); original ECHAM5 code by Roeckner et al. (1995), described in the ECHAM5 documentation (Chap. 6.3 − 6.5 in Roeckner et al.,

155 2003)). The prescribed multi-year monthly mean climatology of SSTs and SIC is an observations based estimate of the years 2000 to 2009 from the Met Office Hadley Center (Rayner et al., 2003). The same climatology was used by Winterstein et al. (2019). Appendix C of Stecher (2024) provides a comparison of the two reference simulations. Overall, the simulation REF-SSTvar reproduces the simulation REF-SSTfix well. The largest differences are in the Southern Hemisphere (SH) polar region,

where the MLO model tends to underestimate the sea ice area of the prescribed climatology, which has been noted for a similar application of the MLOCEAN submodel as well (Stecher et al., 2021).

The perturbation simulations ERFCO$_2$ and ERFCH$_4$ are performed with the same prescribed climatology of SSTs and SICs as REF-SSTfix to assess the so-called fast response and to quantify the ERF and the adjustments following the fixed SST method (e.g., Forster et al., 2016). ERF is defined as the top of atmosphere (TOA) net radiative flux change between the experiment and the reference simulation. The perturbations of CO$_2$ and CH$_4$ are scaled to result in ERFs of similar magnitude, because for a most fair comparison of the climate sensitivity parameters of different perturbation agents, the respective forcings need to be at the same order of magnitude as the climate sensitivity, as it can be dependent on the magnitude of the forcing (e.g., Hansen et al., 2005; Dietmüller et al., 2014). The ERF is targeted to be large enough to cause statistically significant and interpretable feedbacks (Forster et al., 2016), and small enough to be reached with still realistically large perturbations of CO$_2$ and CH$_4$ (Dietmüller et al., 2014; Winterstein et al., 2019). Perturbations of 1.35×CO$_2$ mixing ratios and 2.75×CH$_4$ surface emission fluxes result in ERFs of 1.61±0.16 W m^{-2} and 1.72±0.17 W m^{-2}, respectively (see Tab. 4). The scaling of 1.35×CO$_2$ mixing ratios or 2.75×CH$_4$ surface emission fluxes is applied to all CO$_2$ and CH$_4$ perturbation experiments, respectively. ECCCO$_2$ and ECCCH$_4$ are so-called equilibrium climate change simulations. In these simulations the MLO model accounts for the response of SSTs and SICs. Therefore, the effect of GSAT driven feedbacks is included in these simulations.

In the following, we assess the so-called fast response as the difference between ERFCO$_2$ or ERFCH$_4$ and REF-SSTfix, and the full response as the difference between ECCCO$_2$ or ECCCH$_4$ and REF-SSTvar. The difference between the full and the fast response is assessed as the climate response, which represents the isolated effect of the GSAT change. Similarly, adjustments and feedbacks are defined as the radiative effects corresponding to the fast response and the climate response, respectively. For the analysis, results of 20 simulated years after the spin-up period are used. The spin-up ensures that a quasi-equilibrium is reached and is, therefore, different for the individual simulations according to the simulation set-up. For ERFCH$_4$ the longest spin-up period of 90 years, for ECCCO$_2$ and ECCCH$_4$ 50 years, respectively, and for ERFCO$_2$ 25 years were necessary. Time series of the global mean surface CH$_4$, the total atmospheric masses of CH$_4$ and O$_3$, the TOA radiation balance, and GSAT (for the MLO simulations) were monitored to decide whether an equilibrium is reached. In addition, we assessed the spin-up of the mass of CH$_4$ of the simulation ERFCH$_4$ in more detail. A curve fit was applied to the spin-up period to derive the atmospheric mass of CH$_4$ in equilibrium. The mass of CH$_4$ follows the exponential function of the form $a - b \cdot exp(-t/c)$ closely. The mass of CH$_4$ in the last year of the spin-up, simulation year 90, is about 0.5% smaller than the derived equilibrium estimate (parameter a), and therefore spun-up sufficiently well (see Fig. S14). The derived perturbation lifetime (parameter c) is 21.6 years. We note that the perturbation lifetime is larger than that of the CH$_4$ emission reduction experiment by Staniaszek et al. (2022). As the perturbation lifetime increases with increasing CH$_4$ burden (Holmes, 2018), this can be expected. In addition, model differences and the magnitude of the emission change might play a role.

Table 1. Overview of performed simulations. REF indicates that the respective reference is used, which is 388.4 ppmv for the global mean surface mixing ratio of CO_2, and 625.3 Tg(CH_4) a^{-1} for the CH_4 surface emissions. The prescribed multi-year monthly mean climatology of SSTs and SIC is based on an observations based estimate of the years 2000 to 2009 from the Met Office Hadley Center (Rayner et al., 2003).

simulation name	SST + SIC	CO_2 VMR	CH_4 surface emissions
REF-SSTfix	prescribed	REF	REF
REF-SSTvar	MLO	REF	REF
ERFCO$_2$	prescribed	REF×1.35	REF
ECCCO$_2$	MLO	REF×1.35	REF
ERFCH$_4$	prescribed	REF	REF×2.75
ECCCH$_4$	MLO	REF	REF×2.75

In this study, the CH_4 lifetime is calculated according to Jöckel et al. (2016) as

$$\tau_{CH_4} = \frac{\sum\limits_{b \in B} m_{CH_4}}{\sum\limits_{b \in B} k_{CH_4+OH}(T) \cdot c_{air}(T,p,q) \cdot x_{OH} \cdot m_{CH_4}}, \tag{2}$$

with m_{CH_4} being the mass of CH_4 in [kg], $k_{CH_4+OH}(T)$ the temperature T dependent reaction rate coefficient of the reaction $CH_4 + OH \rightarrow products$ in [cm^3 s^{-1}], c_{air} the concentration of air in [cm^{-3}] and x_{OH} the mole fraction of OH in [mol mol^{-1}] in all grid boxes b $\in$ B. B is the region, for which the lifetime should be calculated, e.g. all grid boxes below the tropopause for the mean tropospheric lifetime. For the CH_4 lifetime calculation a climatological tropopause, defined as tp$_{clim}$= 300 hPa $-$ 215 hPa $\cdot$ $\cos^2(\phi)$, with ϕ being the latitude in degrees north, is used as recommended by Lawrence et al. (2001). The reaction rate coefficient $k_{CH_4+OH}(T)$ is calculated as in the applied kinetic equation system (submodel MECCA), i.e. as

$$k_{CH_4+OH}(T) = 1.85 \times 10^{-20} \cdot T^{2.82} \cdot \exp\left(-\frac{987}{T}\right). \tag{3}$$

2.2 TAGGING

The TAGGING method (Grewe et al., 2017; Rieger et al., 2018) quantifies the contributions of individual source categories to the mixing ratios of tagged tracers. Tagged tracers are O_3, CO, reactive nitrogen compounds (NO$_y$), peroxyacyl nitrate (PAN), NMHCs, OH, and HO$_2$. For computational reasons NMHCs and NO$_y$ are considered with a family approach. For these species or families of species the individual contributions of emission categories or source processes are calculated. In this study O_3 production from the following categories is considered:

– through photolysis of molecular oxygen (O_2) in the stratosphere (O_3 *stratosphere*),

- from emissions of lightning NO_x (O_3 *lightning*),

- from biogenic precursor emissions, mainly soil NO_x and C_5H_8, (O_3 *biogenic*),

210   - from products of the CH_4 decomposition (O_3 *CH_4*),

- from products of the N_2O decomposition (O_3 *N_2O*),

- from biomass burning precursor emissions (O_3 *biomass burning*)

- and from anthropogenic precursor emissions (O_3 *anthropogenic*).

The categories are the same as defined by Grewe et al. (2017), except for the category O_3 *anthropogenic*, which, in our study,
215   combines O_3 production from all anthropogenic emissions, i.e. of the sectors industry, road traffic, shipping and aviation.

The tagged tracers (i.e. the individual contributions) undergo the same processes as the corresponding total species. These are transport, emissions, dry and wet deposition, and chemical production and loss (see Grewe et al. (2017) for details). For the short-lived species OH and HO_2 a steady-state between chemical production and loss is assumed (Rieger et al., 2018). The chemical reaction rates are taken from the submodel MECCA. Effective production and loss is taken into account for
220   O_3, meaning that production and loss terms from a family, which includes all fast exchanges between O_3 and other chemical species, are considered. The diagnostic tool *ProdLoss* (Grewe et al., 2017) is used to identify all reactions that contribute to effective O_3 production and loss in the applied chemical mechanism. The reaction rates of effective O_3 production and loss are then manually grouped into O_3 production and loss rates, depending on which tagged species contributes to O_3 production or loss.

225   **2.3   Quantification of individual radiative effects**

The assessment of radiative effects in this study follows the ERF framework. This means that (rapid radiative) adjustments, which are defined as the TOA net radiative flux change corresponding to changes in the fast response, i.e. independent from GSAT changes, are accounted for as part of the forcing. Thus, ERF is given as the sum of instantaneous radiative forcing (IRF), defined as the net radiative flux change at TOA excluding any adjustment, and the sum of all individual adjustments A_i (e.g.,
230   Smith et al., 2018)

$$ERF = IRF + \sum_i A_i. \tag{4}$$

Consistently, (slow climate) feedbacks are defined as the TOA net radiative flux change induced by atmospheric parameter changes that correspond to the gradually changing GSAT. These feedbacks act to reduce or enhance the associated GSAT change (ΔT) and determine the climate sensitivity parameter λ (units: K / (W m^{-2})), which is the proportionality constant that
235   relates the equilibrium change of GSAT to the ERF as

$$\Delta T = \lambda \cdot ERF. \tag{5}$$

The feedback parameter α is the negative inverse of the climate sensitivity parameter λ ($\alpha = -\frac{1}{\lambda}$; units: W m^{-2} K^{-1}). The feedback parameter quantifies the net radiative flux change at TOA for a given change in GSAT. Under the assumption of linearity it can be decomposed into the radiative contributions of individual processes affected by the change in GSAT, i.e. the individual feedback parameters α_i, so that (e.g., Forster et al., 2021)

$$\alpha = \sum_i \alpha_i = \sum_i \frac{\partial N}{\partial x_i} \frac{dx_i}{dT}, \tag{6}$$

where N is the radiative flux change at TOA induced by the change of an individual variable of the Earth system x_i.

We quantify adjustments and feedbacks corresponding to composition changes of CO_2, CH_4, O_3 and stratospheric H_2O following the method used by Winterstein et al. (2019) and Stecher et al. (2021): Additional simulations are performed with EMAC using the option for multiple diagnostic radiation calls (Dietmüller et al., 2016; Nützel et al., 2024). These simulations are performed (for the sake of saving computational resources) without interactive chemistry, but with prescribed climatologies for the radiatively active trace gases CH_4, CO_2, O_3, N_2O and the chlorofluorocarbons (CFCs) from the simulations REF-SSTfix or REF-SSTvar. SSTs and SICs are prescribed using the same observational based climatology as used for REF-SSTfix (Rayner et al., 2003). Thus, the background climate of the simulations represents reference conditions. The additional simulations are run over 2 years each (plus 1 year spin-up).

In these simulations the first radiation call, P, provides the radiative heating rates that drive the base model, whereas the other radiation calls, D1, D2, ... , are purely diagnostic. The radiation call D1 serves as the reference for the perturbations and receives identical input as P, except for the specific humidity, for which a monthly mean climatology from the respective reference simulation (REF-SSTfix or REF-SSTvar) is used instead of the prognostic specific humidity from the base model. This is necessary, because the radiation calls to calculate the radiative effect of H_2O use monthly mean climatologies of the specific humidity from the sensitivity simulations (see below), and therefore need to be compared to a radiation call, that uses a monthly mean climatology of specific humidity instead of the prognostic, highly variable, specific humidity.

In the other radiation calls (D2, D3, ...) either CO_2, CH_4, O_3 or the specific humidity is replaced by a monthly mean climatology from the sensitivity simulation (either ERFCO2, ECCCO2, ERFCH4 or ECCCH4) to calculate the corresponding radiative effect. For example, to derive the radiative effect of the full response of CH_4 of the CO_2 perturbation, the reference CH_4 climatology in D1 is replaced by the monthly mean CH_4 climatology from ECCCO2 in D2. For O_3 and the specific humidity the radiative effects of changes in the troposphere and in the stratosphere are derived separately. The diagnostic radiation calls include the stratospheric temperature adjustment induced by the respective perturbation following the method of Stuber et al. (2001). Therefore, the radiative effect corresponding to CH_4 (CO_2) from the simulation ERFCH4 (ERFCO2) represents stratospheric adjusted radiative forcing (SARF), i.e. the direct radiative effect of the perturbation including the associated stratospheric temperature adjustment. To define the region in which the stratospheric temperature adjustment is applied, as well as to separate tropospheric and stratospheric radiative effects of O_3 and the specific humidity, the climatological tropopause tp$_{clim}$ is used consistently with the CH_4 lifetime calculation (see Sect 2.1).

There is one methodological difference compared to Winterstein et al. (2019) and Stecher et al. (2021). They used the climatological specified humidity directly in the first prognostic radiation call, which then served as the reference for the

perturbed calls. However, here it was decided to use the prognostic specific humidity in the first radiation call as it is consistent with the model's background meteorology, e.g. the cloud cover. The influence on the calculated radiative effects was tested and found to be up to 1.02% (or 0.004 W m^{-2}) with the maximum deviation for the perturbations of specific humidity, which is negligible in comparison to other uncertainties.

3   Results

3.1   Methane and ozone composition changes following 1.35×CO$_2$ perturbation

In this section, we present the simulation results of the 1.35×CO$_2$ perturbation. Figure 1 shows the annual zonal mean composition changes of CH$_4$ mixing ratios in the simulations ERFCO$_2$ (fast response) and ECCCO$_2$ (full response), and their difference, which is interpreted as the climate response. The fast response is dominated by increasing CH$_4$ mixing ratios in the upper stratosphere and mesosphere. In this region, the cooling to be expected from the CO$_2$ increase (see Fig. S1 in the supplement) leads to the prolongation of the CH$_4$ lifetime. The stratospheric CH$_4$ loss by reaction with OH, Cl, and O(^{1}D) is reduced by about 2% (see Tab. S1 in the supplement). A similar effect has been noted by Dietmüller et al. (2014). In the fast response, tropospheric CH$_4$ shows a slight increase below 2%.

In contrast to the fast response, the full response shows a significant reduction of CH$_4$ mixing ratios in the troposphere and lower stratosphere. As CH$_4$ emission fluxes are prescribed in the simulation set-up and cannot respond to changes in meteorology or composition, any feedback on natural CH$_4$ emissions (e.g., Dean et al., 2018) is suppressed. Therefore, the decrease of CH$_4$ mixing ratios results from enhanced chemical decomposition of CH$_4$, mainly by the oxidation with OH. The tropospheric CH$_4$ lifetime with respect to oxidation by OH shortens by about 7 months (0.56 a or 7.4 %, see Tab. 2). This shortening is a combined result of the direct influence of the temperature on the reaction rate coefficient and of an enhanced abundance of OH. Tropospheric warming increases OH mixing ratios throughout the troposphere with the maximum increase in the tropics (see Fig. S3 in the supplement). Firstly, emissions from lightning NO$_x$ increase by about 0.3 Tg(N) a^{-1} in the climate response (see Tab. 3), which leads to enhanced production of OH. To estimate the effect on the CH$_4$ lifetime, we use the multi-model mean sensitivity of the CH$_4$ lifetime towards lightning NO$_x$ emission change of -4.8% (Tg(N) a^{-1})$^{-1}$ from Thornhill et al. (2021a), which suggest a shortening of the CH$_4$ lifetime due to lightning NO$_x$ emissions by 1.4%. Additionally, the increase in the tropospheric humidity associated with higher temperatures leads to enhanced production of OH.

In addition to the reduction in the troposphere, the CH$_4$ mixing ratios decrease also in the lower stratosphere as part of the full response. As the reaction partners of CH$_4$, namely OH, Cl and O(^{1}D), do not show any significant response in the lower stratosphere (see Fig. S3 for OH), and the stratospheric CH$_4$ loss does not change (see Tab. S1 in the supplement), the decrease is likely a transport effect. Tropospheric air masses with reduced CH$_4$ mixing ratios compared to the reference simulation enter the stratosphere by the upwelling branch of the Brewer-Dobson-Circulation. Tropical upwelling is enhanced in the climate response (see Fig. S13 in the supplement). Dietmüller et al. (2014) noted an increase of CH$_4$ mixing ratios throughout the stratosphere as a result of 2×CO$_2$ due to stratospheric cooling and thereby a slower CH$_4$ oxidation. In addition, enhanced tropical upwelling transports CH$_4$ enriched air in the stratosphere more efficiently. In our setup, the reduction of tropospheric

CH$_4$, which is suppressed in the set-up of Dietmüller et al. (2014) as CH$_4$ mixing ratios are prescribed at the lower boundary, dominates the latter two processes.

Previous studies also found that tropospheric warming leads to increasing OH mixing ratios and correspondingly to the shortening of the CH$_4$ lifetime (e.g., Voulgarakis et al., 2013; Dietmüller et al., 2014; Heimann et al., 2020; Stecher et al., 2021; Thornhill et al., 2021a). The novelty of our study is that the associated reduction of CH$_4$ mixing ratios is simulated explicitly, which was assessed by only a small number of studies so far (Heimann et al., 2020). In our CO$_2$ perturbation experiment, the CH$_4$ lifetime change per unit change of GSAT is -0.51 a K^{-1} or -6.7 % K^{-1}.

Voulgarakis et al. (2013) addressed the sensitivity of the CH$_4$ lifetime towards climate change in the Atmospheric Chemistry and Climate Modeling Intercomparison Project (ACCMIP) model ensemble. In the respective sensitivity simulations the boundary conditions for SSTs, SICs and CO$_2$ were set to RCP8.5 conditions for the years 2030 or 2100, while all other boundary conditions were representative of the year 2000. They found sensitivities of the tropospheric CH$_4$ lifetime of -0.31 $\pm$ 0.14 a K^{-1} (-3.2 $\pm$ 1.0 % K^{-1}) and -0.34 $\pm$ 0.12 a K^{-1} (-3.4 $\pm$ 0.8 % K^{-1}) for the year 2030 and the year 2100 experiments, respectively[1]. The CMIP6 AerChemMIP model ensemble as analyzed by Thornhill et al. (2021a) suggests a sensitivity of the whole-atmosphere CH$_4$ lifetime towards climate change of -0.6 $\pm$ 4.5 % K^{-1} assessed from abrupt 4$\times$ pre-industrial CO$_2$ experiments. The large intermodel spread results from one model that shows an extension of CH$_4$ lifetime as a result to 4$\times$CO$_2$. The three models showing a shortening of CH$_4$ lifetime suggest a sensitivity of -3.2 $\pm$ 0.8 % K^{-1} in close agreement with Voulgarakis et al. (2013).

Our study indicates a larger sensitivity of the CH$_4$ lifetime towards climate change compared to Voulgarakis et al. (2013) and Thornhill et al. (2021a). Possible reasons are the different magnitudes of the perturbations, differences in the simulation set-ups, or the explicit treatment of the CH$_4$ feedback in our study. The similar estimates for the years 2030 and 2100, corresponding to 1.14 K and 4.76 K change of GSAT, respectively[2], by Voulgarakis et al. (2013) suggest that the sensitivity is not highly dependent on the magnitude of the perturbation. Furthermore, the set-ups of individual models in Voulgarakis et al. (2013) and Thornhill et al. (2021a) differ, e.g. with respect to the level of complexity of the chemical mechanism, whether interactive aerosol is used, or through the different treatment of natural O$_3$ precursor emissions. Nevertheless, the present estimate is larger than the estimates of all individual models in Voulgarakis et al. (2013) and Thornhill et al. (2021a), except for two models which do not parameterize the effect of stratospheric O$_3$ on photolysis rates below, which is taken into account here. In the simulation set-ups analyzed by Voulgarakis et al. (2013) and Thornhill et al. (2021a) CH$_4$ mixing ratios are prescribed at the lower boundary in all models, except for the GISS-E2-R model analyzed by Voulgarakis et al. (2013). The lifetime response per unit temperature change derived from GISS-E2-R is comparably weak. GISS-E2-R calculates wetland emissions of CH$_4$ online, presumably also for the climate sensitivity experiments, which makes it difficult to compare the CH$_4$ lifetime response in this model to our study. Nevertheless, compared to the other models, the explicit treatment of the CH$_4$ feedback in our set-up allows for a subsequent feedback on OH and correspondingly for a self-feedback on the CH$_4$ lifetime, which can explain the enhanced sensitivity of the CH$_4$ lifetime towards climate change.

---

[1]Relative estimates were calculated from estimates given in Tables 1 and 4 of Voulgarakis et al. (2013)

[2]Multi-model mean changes of GSAT were calculated from the estimates given in Table 4 of Voulgarakis et al. (2013).

If the CH_4 mixing ratio can not adapt to changes in its lifetime, the corresponding CH_4 equilibrium mixing ratio can be estimated using Eq. 1. The feedback factor f in the equation accounts for the CH_4-OH feedback. In our CH_4 emission driven simulation the CH_4-OH feedback is implicitly included in the simulated response of OH and the CH_4 lifetime, so that using Eq. 1 with $f > 1$ applies the CH_4-OH feedback twice in this case. Eq. 1 indicates a global mean CH_4 equilibrium mixing ratio in the range of 1.61 to 1.66 parts per million volume (ppmv) for $f = [1.19, 1.55]$ for the present changes of the CH_4 lifetime. Thus, it suggests a larger reduction than simulated by the model, which adjusts to a global mean CH_4 equilibrium mixing ratio of 1.69 ppmv (see Tab. 2). However, if the feedback factor is not applied (f=1), Eq. 1 gives 1.68 ppmv, which is in close agreement with the simulated response of CH_4 mixing ratios.

The corresponding response of O_3 is shown in Figure 2. The fast response is dominated by O_3 increases of up to 8% in the middle and upper stratosphere. In these regions, CO_2 induced stratospheric cooling causes slower chemical O_3 depletion (e.g., Rind et al., 1998; Rosenfield et al., 2002; Portmann and Solomon, 2007; Dietmüller et al., 2014; Chiodo et al., 2018). In the lowermost stratosphere, O_3 mixing ratios decrease by up to 4%. This decrease can be explained by the so-called reversed self-healing (Rosenfield et al., 2002; Portmann and Solomon, 2007), which describes the effect that increasing O_3 above leads to a reduction of ultraviolet radiation that reaches the lower stratosphere and consequently to reduced photochemical production of O_3. The effect of transport from the troposphere into the stratosphere is expected to play a minor role in the fast response, as the strength of tropical up-welling is largely determined by the response of SSTs (Garny et al., 2011; Butchart, 2014). The fast response of tropospheric O_3 is smaller than 2%.

The climate response of O_3 is dominated by a reduction of up to 10% in the lowermost tropical stratosphere (see Fig. 2 (c)). Enhanced tropical up-welling transports tropospheric O_3 poor air from the troposphere into the stratosphere more efficiently. This is a robust feature across CCMs (Dietmüller et al., 2014; Nowack et al., 2015; Marsh et al., 2016; Chiodo et al., 2018). In the troposphere, O_3 mixing ratios decrease by up to 6% in the tropics close to the surface and decrease slightly in the upper tropical troposphere.

The pattern of the full response of stratospheric O_3 is qualitatively consistent with previous studies of O_3 changes resulting from a CO_2 perturbation (Dietmüller et al., 2014; Nowack et al., 2015; Marsh et al., 2016; Nowack et al., 2018; Chiodo et al., 2018; Thornhill et al., 2021a). However, the tropospheric response is different here. Most studies using various CCMs consistently show an increase of O_3 in the tropical upper troposphere as part of the full response (Dietmüller et al., 2014; Nowack et al., 2015; Marsh et al., 2016; Nowack et al., 2018; Chiodo et al., 2018). In the studies by Dietmüller et al. (2014) and Nowack et al. (2015, 2018), and presumably also in the studies by Marsh et al. (2016) and Chiodo et al. (2018), CH_4 mixing ratios are prescribed at the lower boundary. Consequently, the negative CH_4 feedback as discussed above can not evolve. This can lead to an overestimation of O_3 produced from products of the CH_4 oxidation and is consistent with the positive response of O_3 in the upper tropical troposphere. In particular, the comparison with the study by Dietmüller et al. (2014) indicates an effect of the CH_4 feedback on O_3 because the EMAC model was used as well in that study.

Using the MESSy submodel TAGGING (Grewe et al., 2017; Rieger et al., 2018) the tropospheric O_3 response is attributed to individual source categories representing different processes of O_3 production. Consistent with the small fast response of total tropospheric O_3 (Fig. 2 (a)), the corresponding response of the individual categories is below 0.5% of the total reference

O$_3$ for all categories, except for *O$_3$ stratosphere* (see Fig. S5 in the supplement). The response of the category *O$_3$ stratosphere* confirms that less O$_3$ is produced via photolysis in the lower tropical stratosphere. Additionally, it indicates enhanced transport from the stratosphere into the troposphere in middle and higher latitudes of the Northern Hemisphere (NH).

375   Figure 3 shows the climate response of individual O$_3$ source categories presented as the difference between the fast and full response of each category in percentage points (p.p.)

$$\Delta O_{3_{\text{cat, climate response}}} = \left(\frac{O_{3_{\text{cat,ECC}}} - O_{3_{\text{cat,REF}}}}{O_{3_{\text{total,REF}}}} \right) - \left(\frac{O_{3_{\text{cat,ERF}}} - O_{3_{\text{cat,REF}}}}{O_{3_{\text{total,REF}}}} \right). \tag{7}$$

The presentation relative to the total reference O$_3$ allows to directly compare the responses of the individual categories to the relative response of total O$_3$ as shown in Fig. 2 (c) and Fig. 3 (a).

380   The climate response of the category *O$_3$ stratosphere* shows significantly enhanced transport of stratospheric O$_3$ into the troposphere in both hemispheres. In the extratropical middle troposphere, O$_3$ mixing ratios increase by up to 1.5% relative to the total reference O$_3$ in the full response, which is the largest positive contribution to the total tropospheric O$_3$ response. This supports current knowledge, as enhanced entry of stratospheric O$_3$ under increasing GHG concentrations has been a robust feature in CCMs (Abalos et al., 2020). The category *O$_3$ stratosphere* is also the largest contributor to the strong reduction in the

385   lowermost stratosphere. The category *O$_3$ lightning* shows a significant increase of up to 1.25% relative to total reference O$_3$ in the middle tropical troposphere. This is consistent with an increase of lightning NO$_x$ emissions by about 0.3 Tg(N) a^{-1} globally (see Tab. 3). Lightning NO$_x$ is emitted mainly in the upper tropical troposphere where convection is strongest (not shown). Biogenic emissions of NO$_x$ and C$_5$H$_8$ increase in the full response as well. Biogenic C$_5$H$_8$ emissions increase strongest in the Amazon region and the Congo river basin, whereas biogenic NO$_x$ emissions increase over land in the tropics and mid

390   latitudes (not shown). However, the zonal mean climate response of *O$_3$ biogenic* is mostly not significant due to competing effects of enhanced precursor emissions and of enhanced chemical loss with H$_2$O. An enhanced sink of O$_3$ via the reaction of O(^{1}D) with H$_2$O, which leads to effective O$_3$ loss, is expected in a warmer and moister troposphere (e.g., Stevenson et al., 2006). The spatial distribution of the tropospheric O$_3$ column shows mainly a reduction over the tropical ocean (see Fig. S7 in the supplement), which is also reflected by the significant reduction between the equator and 30° N in the zonal mean

395   (Fig. 3 (d)). Locally over regions with increasing precursor emissions, e.g. over the Amazon region and the Congo river basin, the tropospheric O$_3$ column increases in the category *O$_3$ biogenic* (see Fig. S7 in the supplement). Anthropogenic and biomass burning emissions are prescribed and are therefore not affected by the CO$_2$ increase. In these categories, decreasing O$_3$ from enhanced loss or reduced O$_3$ production efficiency is shown. The reduction of *O$_3$ anthropogenic* is most pronounced over the tropical ocean, where a decline of O$_3$ due to enhanced loss via H$_2$O is expected (Stevenson et al., 2006; Zanis et al.,

400   2022). The effect of the reduction of *O$_3$ biomass burning* on total O$_3$ is small, since also its absolute contribution is small. In addition to the enhanced sink, reduced O$_3$ production per emitted NO$_x$ could play a role in the latter two categories as O$_3$ precursor emissions from natural categories increase. The category *O$_3$ CH$_4$* shows a reduction throughout the troposphere. This is consistent with the reduction of CH$_4$ mixing ratios, as in the new equilibrium fewer products of the CH$_4$ oxidation are available for O$_3$ production resulting in reduced O$_3$ production in this category. Further, enhanced chemical loss can contribute

405   to the reduction of this category. In the upper tropical troposphere the increase in lightning NO$_x$ emissions counteracts the
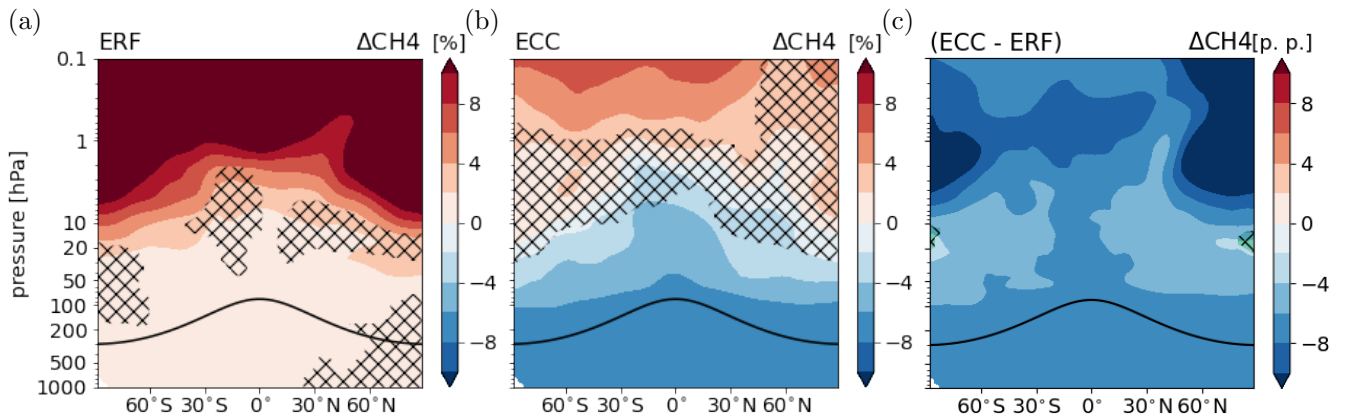
Figure 1. CH_4 response following the CO_2 perturbation: Relative differences between the annual zonal mean CH_4 mixing ratios of sensitivity simulations (a) ERFCO$_2$ (fast response) and (b) ECCCO$_2$ (full response) and their respective reference simulation in [%]. (c) Climate response as difference between the CH_4 responses in panels (a) and (b) in [percentage points (p.p.)]. Non-hatched areas are significant on the 95% confidence level according to a Welch's test based on annual mean values. The solid black line indicates the location of the climatological tropopause.

Table 2. Global annual mean values of tropospheric CH_4 lifetime with respect to oxidation by OH, and CH_4 surface volume mixing ratio for the performed simulations.

	Trop. CH_4 lifetime [a]	CH_4 surface VMR [ppmv]
REF-SSTfix	7.59 ± 0.03	1.82 ± 0.00
REF-SSTvar	7.58 ± 0.03	1.82 ± 0.00
ERFCO$_2$	7.59 ± 0.03	1.82 ± 0.00
ECCCO$_2$	7.02 ± 0.05	1.69 ± 0.00
ERFCH$_4$	14.48 ± 0.04	8.66 ± 0.01
ECCCH$_4$	13.20 ± 0.08	8.05 ± 0.01

The values after the $\pm$ are the corresponding interannual standard deviations based on 20
annual mean values, which are listed to estimate the year to year variability.

effect of the CH_4 decrease by providing enhanced levels of NO_x, which react with the products of the CH_4 oxidation more efficiently. The climate response of O_3 CH_4 is not significant in this region. The climate response in the category O_3 N_2O shows significant decreases in the lower stratosphere and troposphere. In the stratosphere, N_2O mixing ratios increase (not shown) indicating less N_2O decomposition (Dietmüller et al., 2014). Thereby, less nitrogen oxide (NO) is produced to form
410 O_3, which is consistent with the decrease of O_3 formed from N_2O decomposition.

Table 3. Global annual mean emissions of NO_x from lightning, NO_x from biogenic sources, and C_5H_8 from biogenic sources.

	Lightning NO_x [Tg(N) a^{-1}]	Biogenic NO_x [Tg(N) a^{-1}]	Biogenic C_5H_8 [Tg(C) a^{-1}]
REF-SSTfix	5.2 ± 0.1	6.0 ± 0.0	307 ± 3
REF-SSTvar	5.2 ± 0.1	6.0 ± 0.0	306 ± 4
ERFCO$_2$	5.3 ± 0.1	6.0 ± 0.0	307 ± 4
ECCCO$_2$	5.6 ± 0.1	6.4 ± 0.0	338 ± 6
ERFCH$_4$	4.9 ± 0.1	6.0 ± 0.0	306 ± 3
ECCCH$_4$	5.1 ± 0.1	6.4 ± 0.0	337 ± 5

The values after the $\pm$ are the corresponding interannual standard deviations based on 20 annual mean values, which are listed to estimate the year to year variability. The model calculated biogenic C_5H_8 emissions are scaled by a factor of 0.6 before being added to the atmospheric C_5H_8 tracer (see Jöckel et al., 2016). The values shown here include the scaling.
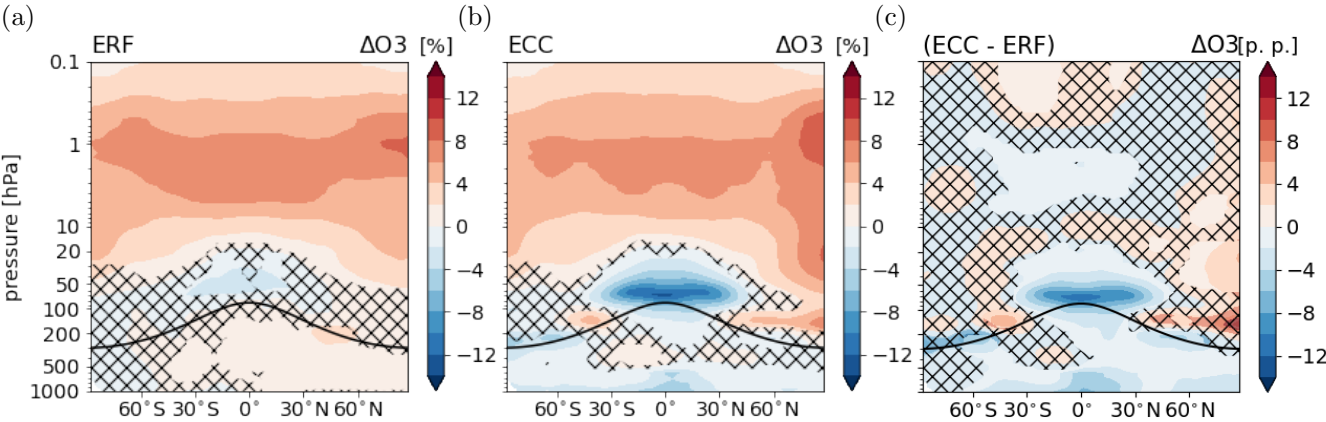
Figure 2. Same as Fig. 1, but for O_3.

3.2 Methane and ozone composition changes following $2.75 \times CH_4$ emission flux perturbation

In this section, we present the simulation results of the $2.75 \times CH_4$ emission flux perturbation. Figure 4 shows the zonal mean distribution of CH_4 mixing ratios of the reference simulation REF-SSTfix and of the two simulations with CH_4 emission fluxes increased by a globally constant factor of 2.75. As expected, CH_4 mixing ratios increase everywhere in the fast response shown in Fig. 4 (b). Hereby, the increase factor of CH_4 mixing ratios is even larger than the increase factor of the emission fluxes. Tab. 2 shows that an increase of CH_4 emissions by a factor of 2.75 results in an increase in the global mean surface CH_4 mixing ratio by a factor of 4.76. This is caused by a large extension of the tropospheric CH_4 lifetime by about 7 years (see Tab. 2). The CH_4 increase reduces the tropospheric OH mixing ratios by up to 60% (see Fig. S3 in the supplement), thereby extending the CH_4 lifetime.
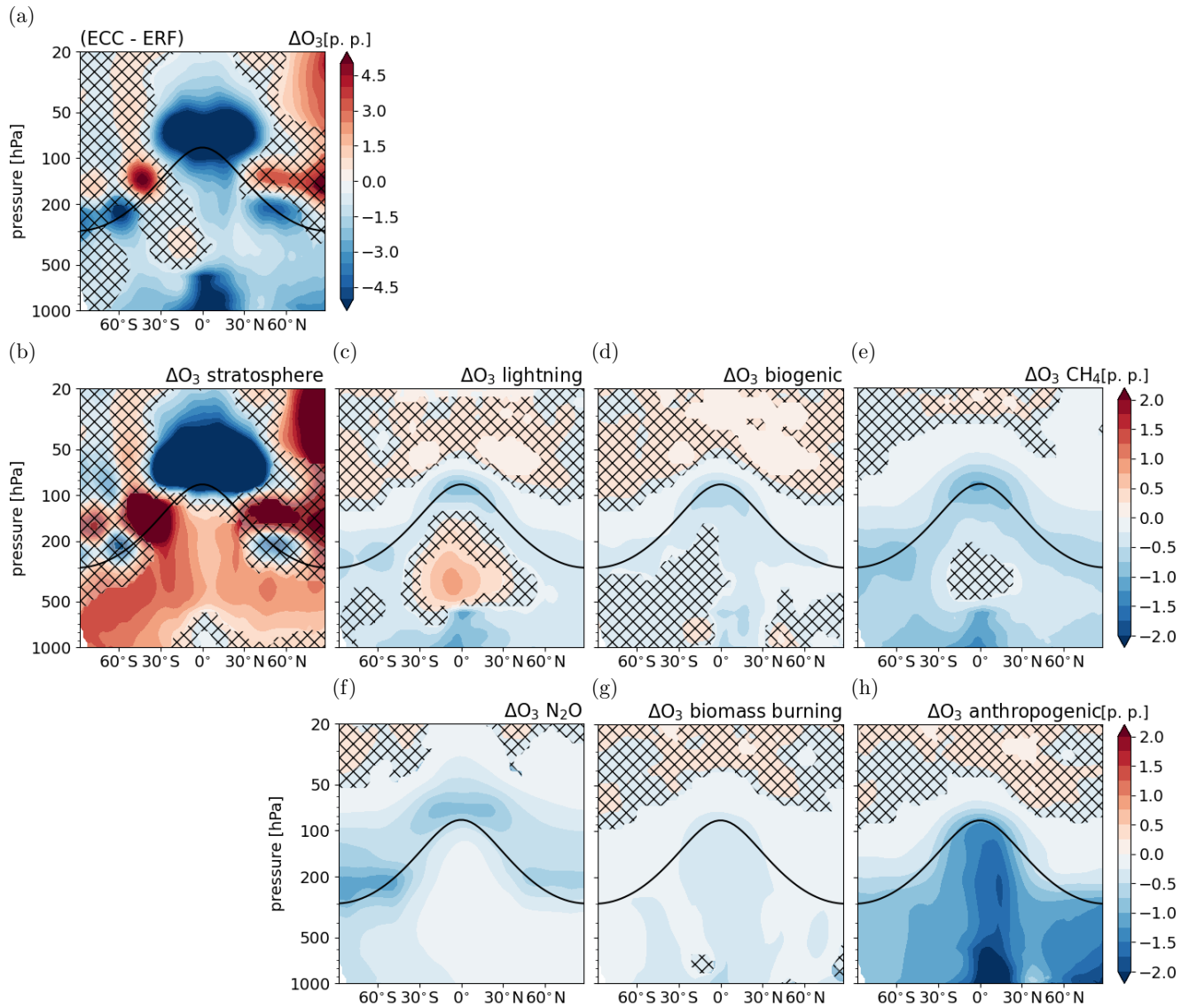
Figure 3. Climate response of tropospheric O_3 following the CO_2 perturbation: (a) response of total O_3 (same as Fig. 2 (c), but differently scaled color levels to better compare with the response in the individual source categories), (b) - (h) response of O_3 in individual categories relative to total reference O_3 ($\Delta O_{3_{\text{cat, climate response}}} = \left(\frac{O_{3_{\text{cat,ECC}}} - O_{3_{\text{cat,REF}}}}{O_{3_{\text{total,REF}}}} \right) - \left(\frac{O_{3_{\text{cat,ERF}}} - O_{3_{\text{cat,REF}}}}{O_{3_{\text{total,REF}}}} \right)$). Non-hatched areas are significant on the 95% confidence level according to a Welch's test based on annual mean values. The solid black line indicates the location of the climatological tropopause.

420   A similar effect was found by Winterstein et al. (2019) who analyzed the fast response of $2\times$ and $5\times CH_4$ surface mixing ratios in a set-up with prescribed CH_4 surface mixing ratios also using EMAC. The magnitude of the present CH_4 perturbation is comparable to their $5\times CH_4$ experiment. In particular, to reach the prescribed CH_4 surface mixing ratios a pseudo surface

emission flux is diagnosed in their set-up. The increase factor of the pseudo flux that corresponds to an increase of $5\times CH_4$ is 2.75 (Stecher et al., 2021), exactly the increase factor of CH_4 surface emissions used in our study. Thus, in our study the

425 increase of emission fluxes results in a close to fivefold increase in the CH_4 surface mixing ratio. The global mean reference CH_4 mixing ratio and the corresponding pseudo emission flux are slightly lower in Winterstein et al. (2019), namely about 1.8 ppmv and 567.7 Tg(CH_4) a^{-1}. Additionally, the spatial distribution of their diagnosed pseudo flux is different and might be unrealistic. The latter two points explain, why the increase factor of CH_4 mixing ratios is not exactly the same in our study. Nevertheless, the results suggest that the relation between the increase in CH_4 emissions and mixing ratios at the lower

430 boundary is consistent, if either the emissions or the mixing ratios are increased.

We derive the feedback factor f (see Eq. 1) from ERFCH$_4$ using two approaches. Firstly, it is calculated from Eq. 12 by Holmes (2018) as $f = \frac{ln(m_1/m_0)}{ln(E_1/E_0)}$. Secondly, it is derived from a curve fit of the function $m(t) = m_0 * [2.75^f + (2.75 - 2.75^f) * exp(-t/(f*\tau)]$ (Holmes, 2018) of the spin-up of the atmospheric mass of CH_4 using the yearly mean CH_4 lifetime with respect to OH oxidation for τ (see Fig. S14). Both approaches suggest $f = 1.55$. However, the derived f is not expected to

435 be representative for CH_4 perturbations of EMAC close to present-day conditions because f increases with increasing CH_4 burden (Holmes, 2018). This might also explain why our estimate of f is at the upper end of previous estimates (Fiore et al., 2009; Voulgarakis et al., 2013; Stevenson et al., 2013; Thornhill et al., 2021b; Stevenson et al., 2020; Sand et al., 2023).

In the stratosphere, CH_4 loss by OH is enhanced due to an increase in stratospheric HO_x, whereas CH_4 loss by Cl is reduced (see Tab. S1 in the supplement). Overall, chemical stratospheric CH_4 loss is increased by 17.5%. However, the increase of CH_4

440 mixing ratios is larger than the increase factor of surface emissions of 2.75 in the whole stratosphere as well.

In the full response, as shown in Fig. 4 (c), CH_4 mixing ratios are lower in comparison to the fast response, as shown in Fig. 4 (b). Similar as in the climate response following the CO_2 perturbation, higher tropospheric temperatures lead to increased production of OH (see Fig. S3 in the supplement). Additionally, the temperature dependent reaction rate coefficient leads to a faster CH_4 oxidation. The corresponding sensitivity of the CH_4 lifetime per unit change of GSAT is -1.09 a K^{-1} or -7.6% K^{-1}

445 (relative to the lifetime in ERFCH$_4$). Both, the absolute and the relative sensitivity, are larger compared to the CO_2 perturbation experiment, which is possibly caused by the different CH_4 conditions in the respective fast responses (ERFCO$_2$ and ERFCH$_4$).

Stecher et al. (2021) analyzed the climate response of the $2\times$ and $5\times$ CH_4 surface mixing ratio experiments corresponding to Winterstein et al. (2019). The sensitivity of CH_4 lifetime per unit change of GSAT corresponding to their $5\times CH_4$ surface mixing ratio perturbation is $\frac{-1.17 \, a}{1.28 \, K} = -0.91$ a K^{-1}, which corresponds to a relative change of -5.9% K^{-1} (relative to the

450 lifetime in their fast response), and is thus less pronounced than the respective value of our study. The major difference between the simulation set-ups is that tropospheric CH_4 mixing ratios can not respond to the lifetime response in the set-up of Stecher et al. (2021). This suggests that in the present study the sensitivity of CH_4 lifetime towards climate change is enhanced, because the CH_4-OH feedback is included in the response of OH and, therefore, in the CH_4 lifetime. The same is indicated by the results of the CO_2 perturbation as discussed above.

455 The response of O_3 is shown in Fig. 5. In the fast response (panel (a)), O_3 mixing ratios increase significantly throughout the troposphere with a maximum increase of up to 60% in the upper tropical troposphere. The CH_4 perturbation leads to enhanced O_3 formation by enhanced production of O_3 precursor species through CH_4 oxidation. In the stratosphere, radiatively induced

cooling (a rapid adjustment) leads to O_3 increases in the middle stratosphere. Above 1 hPa, O_3 mixing ratios decrease due to enhanced catalytic depletion by odd hydrogen (HO_x). HO_x is increased by enhanced production of stratospheric H_2O caused by CH_4 oxidation (see Fig. S2 in the supplement) and also by enhanced formation via the sink reaction of CH_4 with $O(^1D)$. In the lower tropical stratosphere O_3 decreases, which can be explained by the reversed self-healing effect (Rosenfield et al., 2002; Portmann and Solomon, 2007), which is also effective for the CO_2 perturbation (see above). The fast response of O_3 is consistent with the fast response evolving in the comparable $5 \times CH_4$ surface mixing ratio experiment (Winterstein et al., 2019), as the same processes are effective, which are explained in more detail by Winterstein et al. (2019).

Fig. 6 shows the fast response of individual O_3 categories derived using the TAGGING submodel. Shown is the difference between ERFCH$_4$ and REF-SSTfix of one category relative to the total reference O_3

$$\Delta O_{3_{cat}} = \frac{O_{3_{cat,ERF}} - O_{3_{cat,REF}}}{O_{3_{total,REF}}},$$

allowing a direct comparison with the relative response of total O_3. The O_3 mixing ratios increase in all categories except for the category O_3 *stratosphere*. This category shows reduced O_3 production through photolysis of O_2 in the lower stratosphere consistent with the reverse self-healing effect. The increase is strongest in the category O_3 *CH$_4$*, as the CH_4 increase directly leads to the formation of O_3. The increase of this category is most pronounced in the upper tropical troposphere and reaches up to 30% relative to the total reference O_3. The larger abundance of NMHCs and CO also affects O_3 production of the other categories as their reaction with precursors from other categories, in particular NO_x, leads to enhanced O_3 production in the category O_3 *CH$_4$*, but also in the other categories. This effect is largest for the category O_3 *lightning*, which shows O_3 increases of up to 20% relative to the total reference O_3, even though emissions of lightning NO_x decrease by 0.3 Tg(N) a^{-1} globally in the simulation ERFCH$_4$ compared to REF-SSTfix (see Tab. 3). The CH_4 perturbation leads to upper tropospheric/lower stratospheric warming peaking at around 100 hPa in the tropics (see Fig. S1 in the supplement). The higher static stability leads to less convection and thereby to decreasing lightning NO_x emissions. Upper troposphere/lower stratosphere warming following increased CH_4 has been already noted elsewhere and is expected to be even more pronounced if shortwave (SW) absorption by CH_4 is accounted for in the simulation set-up (Modak et al., 2018; Allen et al., 2023). Nevertheless, the enhanced abundance of precursors from CH_4 oxidation lead to enhanced O_3 production in this category. The category showing the third most pronounced increase is O_3 *anthropogenic*. Here, the increase of up to 15% relative to the total reference O_3 is most pronounced in the lower NH, where the contribution of O_3 *anthropogenic* to total O_3 is largest.

The climate response of O_3 shown as the difference between full and fast response (see Fig. 5 (c)) represents the isolated effect of the GSAT response on O_3. It shows a strong reduction of O_3 mixing ratios in the lower tropical stratosphere, which is caused by enhanced tropical up-welling (consistent with the CO_2 simulation). In the Northern polar lower stratosphere, O_3 mixing ratios are enhanced pointing towards strengthened poleward and downward transport (i.e. strengthening of the Brewer-Dobson circulation, see Fig. S13 in the supplement) of stratospheric air masses. In the Southern polar tropopause region the rise of the tropopause in the climate response leads to a large O_3 reduction. This process is also apparent in the NH, albeit less pronounced. Apart from that, the full response of O_3 in the stratosphere is mainly caused by the fast response. The climate response of tropospheric O_3 shows a reduction, except for the tropical middle troposphere, where the response shows a weak,

not significant, increase in the zonal mean. In this region, enhanced emissions of lightning NO_x lead to enhanced O_3 formation (see also discussion of TAGGING results below). The climate response of O_3 is strikingly similar with the climate response pattern resulting from the CO_2 perturbation (see Fig. 2 (c)), even though the fast response is different. The spatial distribution of the climate response of surface O_3 is likewise similar for the CO_2 and the CH_4 perturbation (see Fig. S4).

The similarity of the climate response patterns of O_3 resulting from CO_2 and CH_4 perturbations has been also noted by Stecher et al. (2021). However, the O_3 climate response resulting from their $5 \times CH_4$ mixing ratio increase shows a significant increase of O_3 in the tropical middle troposphere. As already stated, the main difference between their set-up and ours is that the feedback on CH_4 mixing ratios, and thereby also any secondary effects on O_3, is suppressed. As for the CO_2 perturbation, the reduction of CH_4 mixing ratios feeds back on O_3.

Fig. 7 shows the climate response of individual O_3 source categories. It is calculated using Eq. 7 in accordance with the corresponding analysis of the CO_2 perturbation. The patterns of the climate response of the individual categories are overall consistent with those of the CO_2 perturbation.

The category O_3 *stratosphere* increases in the troposphere, indicating enhanced transport of stratospheric O_3 into the troposphere. The increase is significant everywhere, except for the extratropical SH and the lower tropical troposphere. This category contributes strongest to the reduction of O_3 in the lower tropical stratosphere. The category O_3 *lightning* shows increases in the tropical middle troposphere resulting from an increase of the lightning NO_x emissions by 0.2 Tg(N) a^{-1} in ECCCH$_4$ compared to ERFCH$_4$ (see Tab. 3) and decreases in the lower troposphere. Biogenic NO_x emissions increase by 0.37 Tg(N) a^{-1} and biogenic C_5H_8 emissions increase by about 30 Tg(C) a^{-1} as reaction to climate change (see Tab. 3). However, the zonal mean climate response of O_3 in this category is mostly not significant and shows a decrease in the lower tropical and upper NH troposphere (see Fig. 7 (d)). The tropospheric O_3 columns in this category increase locally over the Amazon region and the Congo river basin, where biogenic emissions of C_5H_8 increase strongest, and decrease mostly over the tropical ocean (see Fig. S9 in the supplement). As already mentioned, the sink of O_3 via the reaction of $O(^1D)$ with H_2O is expected to strengthen in a warmer and moister troposphere. Similar as for the CO_2 perturbation, the effects of increased O_3 precursor emissions and the enhanced chemical sink due to a larger abundance of tropospheric H_2O compete in this category. The category O_3 *CH$_4$* decreases everywhere in the zonal mean, except for the tropical middle troposphere. The reduction is consistent with the reduction of CH_4 mixing ratios in the climate response, which leads to a reduced formation of O_3. In addition, the enhanced chemical sink leads to further reduction of O_3. The increase in the tropical middle troposphere coincides with the maximum increase of O_3 production from lightning NO_x emissions, which indicates that enhanced NO_x from lightning reacts with products of the CH_4 oxidation resulting in an increased O_3 production in both categories. The corresponding response of the tropospheric O_3 columns is not significant in the tropics, because of the counteracting responses in the lower and middle troposphere, but shows a significant decrease in the extra-tropics (see Fig. S9 in the supplement). The categories with prescribed O_3 precursor emissions, O_3 *biomass burning* and O_3 *anthropogenic*, show decreased O_3 mixing ratios throughout the troposphere (see Fig. 7 (g) and (h)), consistently with the climate response resulting from the CO_2 perturbation. Additionally, reduced O_3 production per emitted molecule NO_x can play a role as O_3 precursor emissions of natural categories increase.
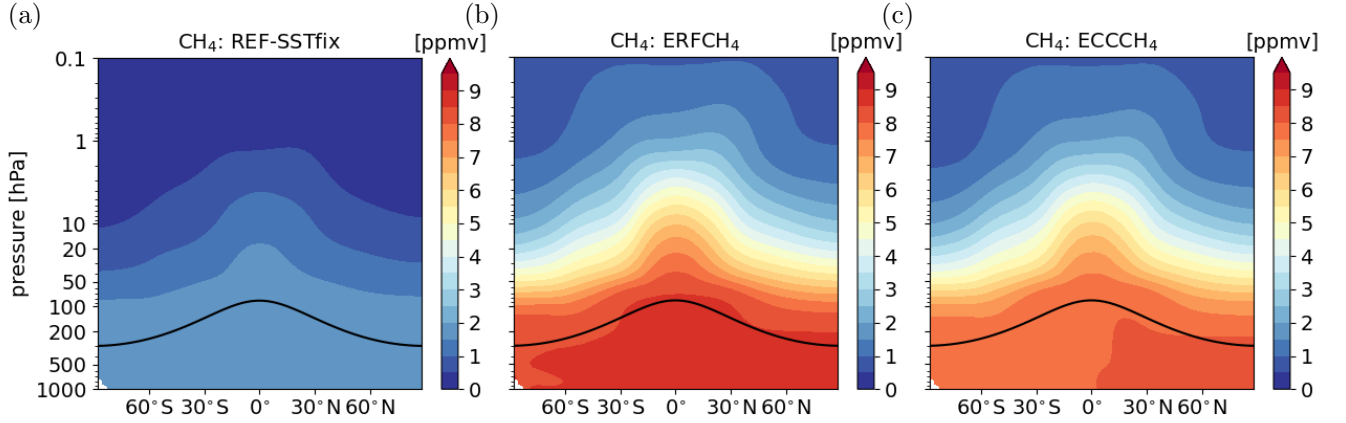
Figure 4. Annual zonal mean distribution of CH_4 mixing ratios in simulation (a) REF-SSTfix, (b) ERFCH$_4$ (fast response) and (c) ECCCH$_4$ (full response) in [ppmv].
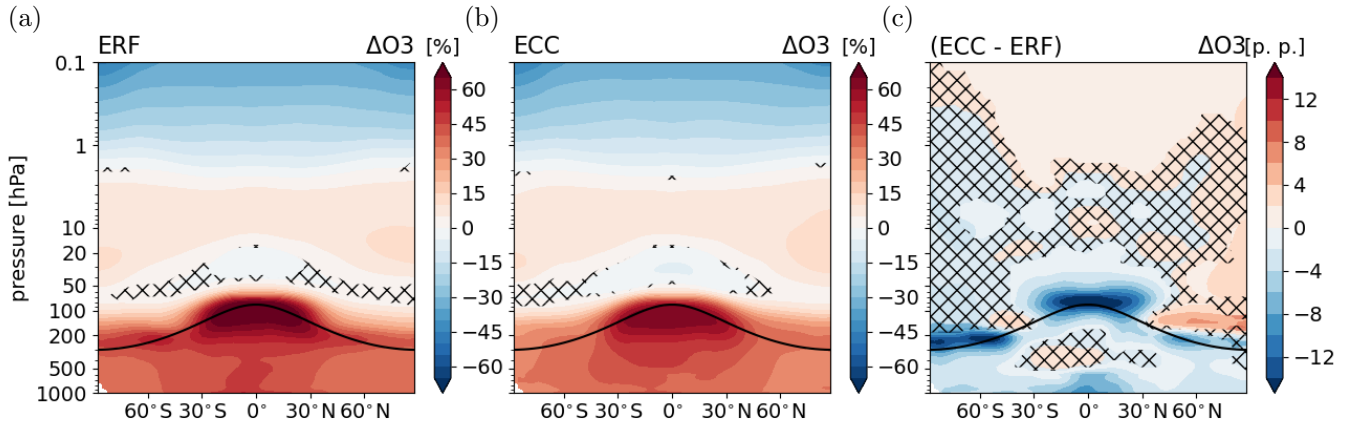
Figure 5. O_3 response following the CH_4 perturbation (same as Fig. 2, but for the CH_4 perturbation): Relative differences between the annual zonal mean O_3 mixing ratios of sensitivity simulations (a) ERFCH$_4$ (fast response) and (b) ECCCH$_4$ (full response) and their respective reference simulation in [%]. (c) Climate response as difference between the O_3 responses in panels (a) and (b) in [percentage points (p.p.)]. Non-hatched areas are significant on the 95% confidence level according to a Welch's test based on annual mean values. The solid black line indicates the location of the climatological tropopause.
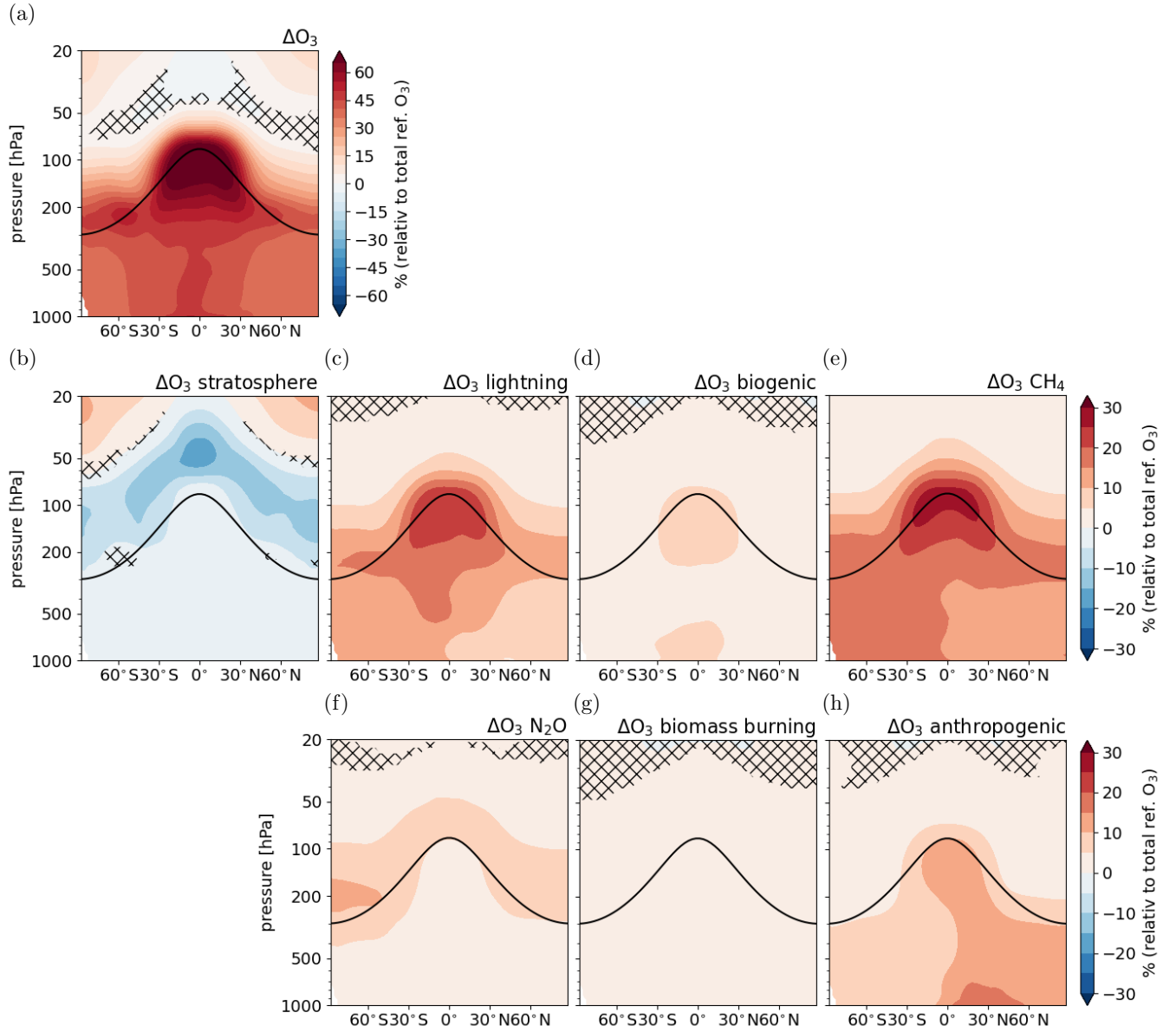
Figure 6. Fast response of tropospheric O_3 following the CH_4 perturbation: (a) response of total O_3 (same as Fig. 4 (a), but differently scaled colour levels to better compare with the response in the individual categories), (b) - (h) response of O_3 in individual source categories relative to total reference O_3 ($\Delta O_{3_{cat}} = \frac{O_{3_{cat,ERF}} - O_{3_{cat,REF}}}{O_{3_{total,REF}}}$). Non-hatched areas are significant on the 95% confidence level according to a Welch's test based on annual mean values. The solid black line indicates the location of the climatological tropopause.
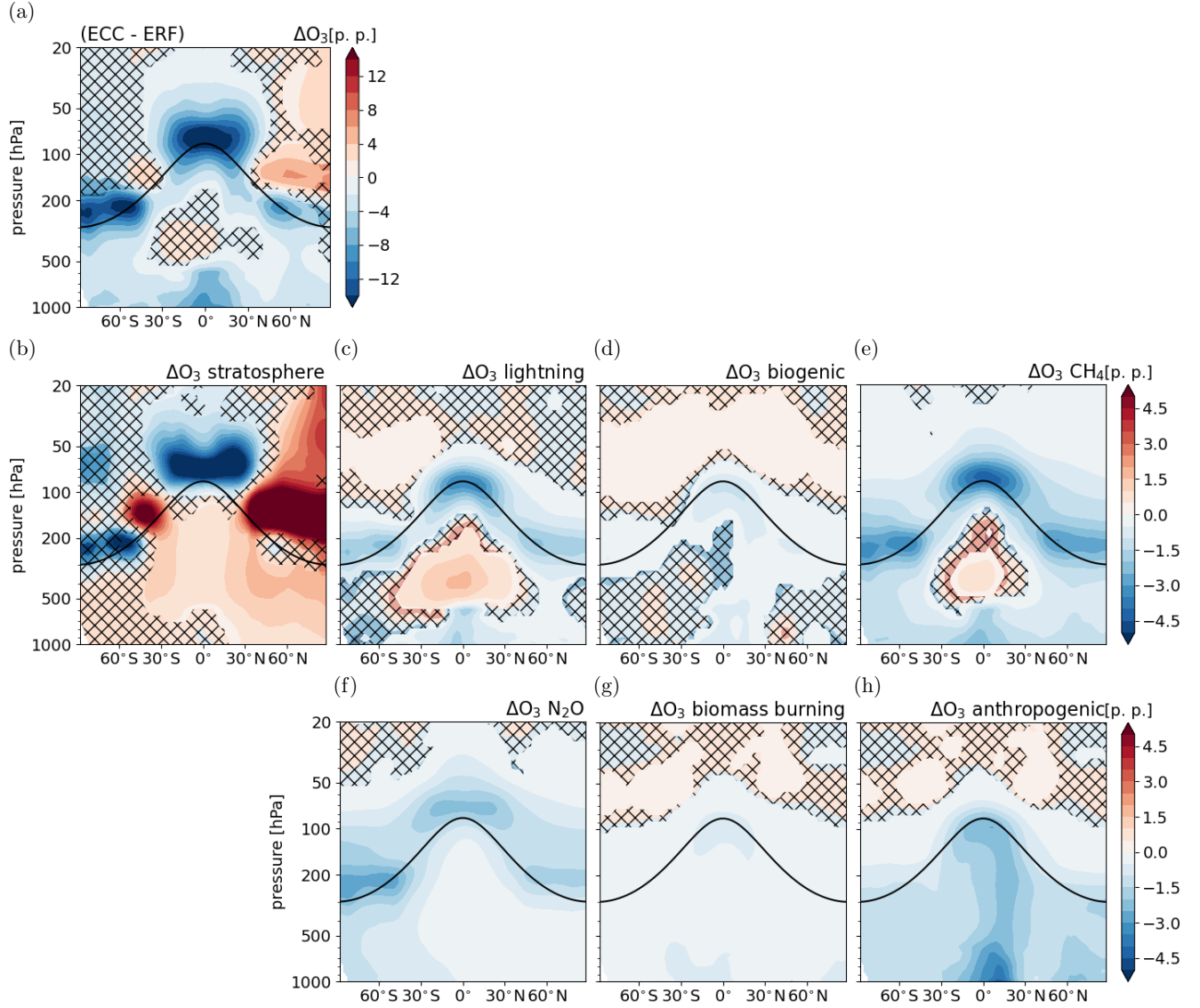
Figure 7. Climate response of tropospheric O_3 following the CH_4 perturbation (same as Fig. 3, but for the CH_4 perturbation): (a) response of total O_3 (same as Fig. 5 (c), but differently scaled colour levels to better compare with the response in the individual categories), (b) - (h) response of O_3 in individual source categories relative to total reference O_3 ($\Delta O_{3\text{cat, climate response}} = (\frac{O_{3\text{cat,ECC}} - O_{3\text{cat,REF}}}{O_{3\text{total,REF}}}) - (\frac{O_{3\text{cat,ERF}} - O_{3\text{cat,REF}}}{O_{3\text{total,REF}}})$). Non-hatched areas are significant on the 95% confidence level according to a Welch's test based on annual mean values. The solid black line indicates the location of the climatological tropopause.

3.3 Radiative effects and climate sensitivity

Table 4 shows results for the total SARF, ERF, ΔGSAT and the associated climate sensitivity parameters λ, as well as individual radiative effects corresponding to the composition changes of CH_4, O_3 and stratospheric H_2O. ERF includes physical and chemical adjustments, whereas SARF represents the radiative effect of the CO_2 or CH_4 composition change and the corresponding stratospheric temperature adjustment only.

For the CO_2 perturbation, the estimate of ERF is smaller than SARF, but the difference is not significant due to the large statistical uncertainty associated with ERF (e.g, Forster et al., 2016). Along with this, the climate sensitivity parameter based on ERF, λ_{ERF}, is larger compared to λ_{SARF}, but the difference is not statistically significant either. In contrast, for the CH_4 perturbation, the estimate of ERF of 1.72 ± 0.17 W m^{-2} is considerably larger than SARF, which is estimated at 0.51 W m^{-2}. The estimate of SARF reproduces the result of the comparable 5$\times$CH$_4$ mixing ratios experiment with the EMAC model (Winterstein et al., 2019). However, the radiative effect of CH_4 is known to be underestimated by the used radiative transfer scheme (Winterstein et al., 2019; Nützel et al., 2024). For instance, using the formula by Etminan et al. (2016)[3] for the present CH_4 perturbation a SARF of about 1.7 W m^{-2} is derived. The underestimation of the radiative effect of CH_4 affects the estimate of ERF as well. Under the assumption that all other adjustments remain the same, only the direct contribution of CH_4 is exchanged, which results in an ERF of about 2.9 W m^{-2}. This considerably larger ERF suggests a correspondingly larger response of GSAT as well.

As illustrated by Tab. 4, chemical adjustments play a minor role for the CO_2 perturbation. The fast response of stratospheric O_3 induces a negative adjustment of -0.034 W m^{-2}, whereas the fast response of tropospheric O_3 induces a positive adjustment of 0.012 W m^{-2}. The adjustment of tropospheric CH_4 is negligible, whereas stratospheric CH_4 induces a small positive adjustment due to its increase in the stratosphere and associated local radiative cooling. H_2O increases in the lowermost stratosphere by up to 5% (see Fig. S2 in the supplement), which leads to a positive adjustment of 0.015 W m^{-2}. The change of H_2O in the lowermost stratosphere is largely driven by a change of the tropical cold point temperature (CPT) (see Fig. S10). For the CO_2 perturbation, chemical production of H_2O in the stratosphere is slightly reduced up to about 2 hPa. Thus, the adjustment of stratospheric H_2O is unlikely to be chemically induced. To summarize, interactive chemistry dampens the ERF of the CO_2 perturbation by about -1.3%, mainly by the effect of stratospheric O_3.

For the CH_4 perturbation, chemical adjustments of O_3 and stratospheric H_2O are important contributions to the ERF. The adjustment of tropospheric O_3 is 0.64 W m^{-2}, and that of stratospheric O_3 is 0.16 W m^{-2}. In addition, the adjustment of stratospheric H_2O is estimated at 0.51 W m^{-2}. The CH_4 perturbation leads to relative increases of H_2O up to 250% in the upper stratosphere and mesosphere (see Fig. S2 in the supplement) because the increased abundance of CH_4 leads to enhanced production of H_2O by CH_4 oxidation. Additionally, warming of the tropical cold point (see Fig. S9) leads to reduced dehydration of upwelling air parcels, and thus to an increased abundance of H_2O in the lower stratosphere. The zonal mean warming of the tropical cold point is 1.5 K and thereby more pronounced than in the respective CO_2 experiment. The CH_4

---

[3]The CH_4 mixing ratios of simulation ERFCH4 are outside of the range tested to derive the formula of Etminan et al. (2016), but the formula can still provide a rough estimate for the CH_4 radiative effect.

perturbation induces a direct radiative heating at the tropical cold point of up to 1 K (see Fig. S12 in the supplement), and the response of stratospheric O_3 leads to additional radiative heating of about 1.5 K in this region (see Fig. S12 in the supplement).

560 To summarize, the adjustments of O_3 and stratospheric H_2O enhance the ERF of the CH_4 perturbation by 1.31 W m^{-2}. The estimates of the adjustments of O_3 and stratospheric H_2O are consistent with the results of the comparable 5×CH_4 mixing ratios experiment (Winterstein et al., 2019, see also column 3 in Tab. 4).

The feedback parameters represent the radiative effects induced by changes in composition related to the climate response, i.e. to the isolated effect of GSAT changes. They are, as usual, given in W m^{-2} K^{-1}, i.e., normalized by the corresponding
565 GSAT response. For both perturbation types, CO_2 and CH_4, the feedbacks of CH_4 and O_3 are negative, which means that they dampen the resulting temperature change. The feedback parameter corresponding to the CH_4 reduction in the CO_2 perturbation experiment is -0.025 W m^{-2} K^{-1}. As already mentioned, it is known that the direct radiative effect of CH_4 is underestimated by the used radiative transfer scheme (Winterstein et al., 2019; Nützel et al., 2024). Therefore, we additionally calculate the feedback parameter for the same change of CH_4 mixing ratios, but with the PSrad radiation scheme (Pincus and Stevens, 2013;
570 Nützel et al., 2024), using otherwise the same methodology (see Sect. 2.3). With PSrad, the CH_4 feedback is estimated at -0.041 W m^{-2} K^{-1} implying a more pronounced negative radiative feedback. Applying the formula of Etminan et al. (2016) for the change of CH_4 mixing ratio diagnosed from the simulation suggests a radiative effect of -0.059 W m^{-2}, which corresponds to a feedback parameter of -0.054 W m^{-2} K^{-1}. Previous estimates of the CH_4 feedback have been derived offline from the change of atmospheric CH_4 lifetime, and range from -0.014±0.067 W m^{-2} K^{-1} (Thornhill et al., 2021a, if the estimates for
575 changes of biogenic volatile organic compounds, lightning NO_x and meteorology are combined[4]), -0.03±0.01 W m^{-2} K^{-1} (Heinze et al., 2019) to -0.036 W m^{-2} K^{-1} (Dietmüller et al., 2014). Our estimate using the PSrad scheme is at the upper end of previous estimates, but in the range of estimates from individual models analyzed by Thornhill et al. (2021a).

For the CH_4 perturbation, the feedback associated with the reduction of CH_4 mixing ratios in the full response in comparison to the fast response is -0.019 W m^{-2} K^{-1}. Using the PSrad radiation scheme with otherwise the same method, the feedback pa-
580 rameter is estimated at -0.089 W m^{-2} K^{-1} suggesting a clearly larger influence. The radiative feedback of CH_4 corresponding to the 5× CH_4 mixing ratio experiment (Winterstein et al., 2019; Stecher et al., 2021) does not include the reduction of CH_4 in the troposphere. The corresponding feedback parameter indicates a small positive feedback, caused by the larger mixing ratios of CH_4 in the stratosphere in the full response compared to the fast response (Stecher et al., 2021).

The feedback parameters corresponding to O_3 changes in the troposphere and stratosphere are both negative and add to
585 total feedback parameters of -0.039 W m^{-2} K^{-1} for the CO_2 perturbation, and -0.054 W m^{-2} K^{-1} for the CH_4 perturbation. Previous studies of the O_3 feedback resulting from CO_2 perturbations have assessed the full response in contrast to the climate response. The feedback parameter corresponding to the full response, i.e. including the adjustment, is -0.059 W m^{-2} K^{-1} in our study. Previous estimates range from -0.015 W m^{-2} K^{-1} and -0.022 W m^{-2} K^{-1} (Dietmüller et al., 2014), -0.018 W m^{-2} K^{-1} (Marsh et al., 2016), -0.046±0.018 W m^{-2} K^{-1} (Thornhill et al., 2021a), to -0.12 W m^{-2} K^{-1} (Nowack et al., 2015, if a
590 corresponding GSAT response of 5.75 K is assumed). The feedback parameter of total O_3 in the present study lies in the

---

[4]If the model CESM2-WACCM, which projects a prolongation of CH_4 lifetime with climate change, is excluded, the CH_4 feedback is estimated at -0.053±0.010 W m^{-2} K^{-1}. The given uncertainties are standard deviations across models.

range of previous estimates, but, notably, is more pronounced than the estimate by Dietmüller et al. (2014), who also used the EMAC model. Part of the difference can be explained by the different sign of the feedback of tropospheric O_3. Dietmüller et al. (2014) found a positive feedback parameter of 0.008 W m^{-2} K^{-1} to 0.009 W m^{-2} K^{-1} for tropospheric O_3 compared to the negative feedback parameter in this study. The reduction of tropospheric CH_4 mixing ratios leads to reduced O_3 production and thereby modifies the response of O_3 as discussed above. This indirect effect on O_3 is a consequence of applying emission fluxes instead of a prescribed lower boundary mixing ratio for CH_4. In addition, also the negative feedback of stratospheric O_3 is more pronounced in this study, which might be explained by the different magnitude of the perturbations. Dietmüller et al. (2014) noted differences between their $2\times$ and $4\times CO_2$ experiments. Therefore, deviations for the $1.35\times CO_2$ in this study can be expected. In addition, the different vertical resolution of the simulation set-ups might affect the response of stratospheric O_3. The results of the $5\times CH_4$ mixing ratio experiment by Stecher et al. (2021) do not indicate a significant feedback of total O_3. This suggests that the reduction of CH_4 mixing ratios in the full response drives the negative O_3 feedback.

As explained above, the scaling factors of the CO_2 and CH_4 increase are chosen so that the resulting ERFs are comparable to allow an optimal comparison of the climate sensitivity of the two perturbation types, as the latter can depend on the magnitude of the radiative perturbation (e.g., Hansen et al., 2005; Dietmüller et al., 2014). The estimates of the climate sensitivity parameter based on ERF, λ_{ERF}, are identical for the CO_2 and CH_4 perturbations of this study. In contrast, the climate sensitivity parameters based on SARF, λ_{SARF}, differ significantly between the CH_4 and the CO_2 perturbation. This finding confirms the results of previous studies that the climate sensitivity is in general less dependent on the type of perturbation for ERF (e.g., Richardson et al., 2019). The use of λ_{ERF} as climate sensitivity parameter to obtain an efficacy close to unity for the CH_4 perturbation is more important in this study compared to Richardson et al. (2019), because of the effect of interactive chemistry, which leads to larger differences between SARF and ERF for the CH_4 perturbation.

The estimate of λ_{ERF} of 0.68$\pm$0.08 K / (W m^{-2}) is smaller than the corresponding estimate of the $5\times CH_4$ mixing ratio experiment of 0.72$\pm$0.07 K / (W m^{-2}) (Stecher et al., 2021). This suggests a reduction of the climate sensitivity parameter caused by the explicit simulation of the CH_4 reduction which would be physically consistent with the negative feedbacks of O_3 and CH_4 in this study. The difference between the two estimates is, however, not statistically significant.

4   Discussion and Conclusions

In this study, we assess the feedback of atmospheric CH_4 resulting from changes in its chemical sink, which is mainly by oxidation with OH and, which is influenced by temperature and the chemical composition of the atmosphere. We present results from numerical simulations with the CCM EMAC perturbed by either $1.35\times CO_2$ mixing ratio or $2.75\times CH_4$ emission flux increase. The scaling factors were chosen to reach a comparable ERF for both perturbation agents. EMAC is used in a CH_4 emission flux driven setup, which allows the atmospheric CH_4 mixing ratio to adjust to changes of the chemical sink without constraints.

The increase of CH_4 emissions by a globally constant factor of 2.75 corresponds to an increase of the global mean CH_4 surface mixing ratio by a factor of 4.76. The larger increase of the CH_4 mixing ratio compared to the emissions is caused

Table 4. Estimates of total SARF, ERF, ΔGSAT and the corresponding climate sensitivity parameters λ, as well as adjustments and feedbacks of individual composition changes of CH_4, O_3 and stratospheric H_2O. ERF includes physical and chemical adjustments, whereas SARF represents the radiative effect of the CO_2 or CH_4 composition change and the corresponding stratospheric temperature adjustment only. The climate sensitivity parameters λ_{SARF} and λ_{ERF} are calculated using SARF or ERF, respectively. Adjustments are calculated as the radiative flux changes of the fast response (in W m^{-2}). Feedbacks are calculated as the difference of radiative flux changes between the full and the fast response divided by the corresponding change of global surface air temperature ΔGSAT (in W m^{-2} K^{-1}). The radiative effects of individual composition changes include the corresponding stratospheric temperature adjustment (Stuber et al., 2001). All radiative estimates are evaluated at TOA. In addition, the estimates of the 5$\times$CH$_4$ volume mixing ratio experiments analyzed by Winterstein et al. (2019) and Stecher et al. (2021) are shown in the third column.

Perturbation		**1.35$\times$CO$_2$ VMR** ERFCO$_2$ / ECCCO$_2$	**2.75$\times$CH$_4$ emissions** ERFCH$_4$ / ECCCH$_4$	**5$\times$CH$_4$ VMR** (Winterstein et al., 2019; Stecher et al., 2021)
SARF	[W m^{-2}]	1.71	0.51	0.51
ERF	[W m^{-2}]	1.61$\pm$0.16	1.72$\pm$0.17	1.79$\pm$0.17
ΔGSAT	[K]	1.09$\pm$0.06	1.17$\pm$0.06	1.28$\pm$0.04
λ_{SARF}	[K / W m^{-2}]	0.64$\pm$0.03	2.30$\pm$0.11	2.49$\pm$0.08
λ_{ERF}	[K / W m^{-2}]	0.68$\pm$0.07	0.68$\pm$0.08	0.72$\pm$0.07
Adjustments	[W m^{-2}]			
O$_3$ trop.		0.012	0.64	0.56
O$_3$ strat.		-0.034	0.16	0.20
O$_3$ total		-0.022	0.81	0.76
CH$_4$		<0.001	-	-
H$_2$O strat.		0.015	0.51	0.55
Feedbacks	[W m^{-2} K^{-1}]			
O$_3$ trop.		-0.023	-0.029	0.005
O$_3$ strat.		-0.016	-0.025	-0.006
O$_3$ total		-0.039	-0.054	-0.001
CH$_4$		-0.025	-0.019	0.004
CH$_4$ using PSrad		-0.041	-0.089	-
H$_2$O strat.		0.15	0.11	0.079

Values after the $\pm$ sign are 2$\times$ the standard error of the mean calculated on the basis of 20 annual mean values, which approximate the corresponding 95% confidence intervals. The standard errors for the climate sensitivity parameters are calculated from the standard error of the corresponding radiative forcing std_err_{RF} and the standard error of ΔGSAT $std\_err_{\Delta GSAT}$, as $std\_err_\lambda = (\sqrt{\frac{std\_err_{RF}^2}{RF^2} + \frac{std\_err_{\Delta GSAT}^2}{\Delta GSAT^2}} \cdot \frac{\Delta GSAT}{RF})$. The method to derive stratospheric adjusted radiative estimates does not account for interannual variability, which is why no uncertainty estimates are provided for the respective estimates.

by a strong reduction of tropospheric OH, which leads to the extension of the tropospheric CH$_4$ lifetime. A similar effect was
625   found by Winterstein et al. (2019), who analyzed the response of 5$\times$CH$_4$ mixing ratios using a comparable set-up of the EMAC

model, but with prescribed CH_4 surface mixing ratios. In particular, to reach the $5 \times CH_4$ mixing ratio increase, a pseudo surface emission flux is calculated in their set-up. The increase factor of the pseudo flux that corresponds to an increase of $5 \times CH_4$ is 2.75 (Stecher et al., 2021), exactly the scaling factor of CH_4 surface emissions used in this study. To summarize, reduced chemical decomposition enhances the increase of the CH_4 mixing ratios compared to the emissions. The relation between the increase of CH_4 mixing ratios and CH_4 emissions appears to be robust, if either the mixing ratio or the emissions are increased.

We separately assess the so-called fast response in CO_2 and CH_4 perturbation simulations with prescribed SSTs and SICs, and the full response in simulations coupled to a MLO model. The CO_2 perturbation affects the chemical composition only indirectly through temperature changes. In the fast response, radiatively induced cooling in the stratosphere causes slower chemical depletion and leads therefore to increasing mixing ratios of O_3 and CH_4. In particular, our results show that the well-known increase of upper and middle stratospheric O_3 (e.g., Dietmüller et al., 2014; Nowack et al., 2015; Marsh et al., 2016; Chiodo et al., 2018) is part of the fast response, and not related to the associated tropospheric warming. The CH_4 emission increase directly influences the chemical composition in the troposphere and stratosphere. The fast response patterns of O_3 and stratospheric water vapour are consistent to the changes following the $5 \times CH_4$ mixing ratio increase (Winterstein et al., 2019) as expected from the comparable magnitude of CH_4 mixing ratio increase.

Despite the different effect on the chemical composition in the fast response, the isolated effect of GSAT changes induced by either the CO_2 or the CH_4 increase is consistent. Tropospheric warming shortens the atmospheric lifetime of CH_4. The corresponding reduction of CH_4 mixing ratios is explicitly simulated by the used CH_4 emission flux driven set-up. The explicit reduction of CH_4 mixing ratios allows for secondary feedbacks on OH and O_3.

Firstly, the CH_4 lifetime response implicitly includes the CH_4-OH feedback. The sensitivities of the CH_4 lifetime per unit change of GSAT are -6.7 % K^{-1} for $1.35 \times CO_2$ and -7.6 % K^{-1} for $2.75 \times CH_4$, which is larger compared to previous CCM results using prescribed CH_4 mixing ratios at the lower boundary (Voulgarakis et al., 2013; Thornhill et al., 2021a; Stecher et al., 2021). The results of the comparable CH_4 increase experiment with prescribed CH_4 surface mixing ratios (Stecher et al., 2021) provide a clear indication that the lifetime change per temperature change is larger in the CH_4 emission driven set-up. A comparable CO_2 increase simulation using EMAC with prescribed CH_4 surface mixing ratios is not available, but the comparison to the results of other CCMs (Voulgarakis et al., 2013; Thornhill et al., 2021a) indicates the same effect (see Sect. 3.1). Estimates of the CH_4 lifetime change per temperature change from other CCMs driven by prescribed CH_4 emission fluxes would be helpful to verify the influence of CH_4 emission fluxes in comparison to prescribing CH_4 at the lower boundary. Additionally, the multi-model differences of the CH_4 lifetime change per unit change of GSAT are large (Voulgarakis et al., 2013; Thornhill et al., 2021a) and it would be valuable to identify reasons behind CCM differences in future studies.

Secondly, the reduction of CH_4 mixing ratios results in reduced formation of O_3 in the troposphere. This leads to substantial differences in the climate response of tropospheric O_3 between this study and previous work using prescribed CH_4 mixing ratios at the lower boundary (Dietmüller et al., 2014; Nowack et al., 2015; Marsh et al., 2016; Nowack et al., 2018; Chiodo et al., 2018; Stecher et al., 2021). The latter studies consistently show an increase of O_3 mixing ratios in the tropical upper troposphere, whereas in this study the response is either insignificantly weak or indicates a reduction of O_3 mixing ratios in this region. An attribution method is used to identify and quantify the processes that influence tropospheric O_3 under

climate change: Stronger stratosphere - troposphere exchange and larger natural emissions of O_3 precursors lead to increases in tropospheric O_3, whereas enhanced chemical loss caused by the increased tropospheric humidity and the reduction of CH_4 mixing ratios lead to decreases. The contribution of the individual processes depend on the representation of the process of the model. For instance, the representation of O_3 precursor emissions from natural sources is model dependent (e.g., Voulgarakis et al., 2013; Stevenson et al., 2020; Zanis et al., 2022). The climate response of lightning NO_x emissions is uncertain so that even the sign of the projected change depends on the used parameterization (Finney et al., 2016, 2018; Zanis et al., 2022). This has implications for the climate response of tropospheric O_3, for which changed lightning NO_x emissions are found to be an important contribution. Most schemes used in CCMs to date project increasing lightning NO_x emissions in response to tropospheric warming (Voulgarakis et al., 2013; Finney et al., 2016), which is in accordance with the results of this study, whereas a more sophisticated lightning NO_x parameterization indicates a decrease of lightning NO_x emissions (Finney et al., 2018). The spatial distribution of increases of biogenic C_5H_8 emissions over the Amazonian region and the Congo river basin are in qualitative agreement with the climate response of biogenic emissions simulated by other CCMs (Zanis et al., 2022, see their Fig. S6). We expect the contribution of biogenic emission changes on O_3 to be more important than diagnosed by the used version of the TAGGING method, as it underestimates the influence of C_5H_8 emissions on the diagnostic tracer O_3 *biogenic*. The NMHC emissions are scaled by the number of C-atoms in the molecule, i.e. 5 for C_5H_8, before they are added to the NMHC family tracer, which was not done in the case of the online calculated biogenic C_5H_8 emissions. We expect that this issue influences the quantitative response of the category O_3 from biogenic sources, more precisely that changes of O_3 *biogenic* caused by changes in C_5H_8 emissions are underestimated. However, we do not expect that the response patterns and general findings would change. Therefore, and due to the computational costs of the simulations, it was decided to not repeat the simulations. We also want to stress that this issue affects the diagnostic TAGGING results only, but not the total O_3 response. Furthermore, biogenic emissions of C_5H_8 depend on the underlying vegetation, which is expected to interact with changes in e.g. climate, atmospheric CO_2 abundance, tropospheric O_3 or land use change (e.g., Zhou et al., 2018; Vella et al., 2023), but such interactions are not included in the used set-up. In addition, droughts can inhibit the substrate supply and thereby reduce biogenic C_5H_8 emissions (e.g., Wang et al., 2022). A respective representation of the impact of droughts on C_5H_8 emissions is not included in the used model version.

We calculate the radiative effects that correspond to the composition changes of CH_4, O_3 and stratospheric H_2O. Our results confirm that chemical adjustments of O_3 and stratospheric H_2O are important contributions to the ERF of the CH_4 perturbation. Therefore, ERF is significantly larger than SARF, which represents the direct radiative effect of CH_4 including the associated stratospheric temperature adjustment. The individual adjustments are in agreement with the estimates of the $5\times CH_4$ mixing ratio experiment (Winterstein et al., 2019).

Chemical adjustments play a minor role in the CO_2 case. Here, stratospheric O_3 induces a negative adjustment, which reduces the ERF by about -1.3%. Previous studies defined the full response of O_3 as its feedback (Dietmüller et al., 2014; Nowack et al., 2015; Marsh et al., 2016). Our results show that under the ERF framework large parts of the stratospheric O_3 change is to be regarded as an adjustment. Further, our results do not indicate that ERF is significantly different from SARF for

the CO_2 perturbation, which is in accordance to simulation results, which account for physical adjustments only (Smith et al., 2018).

The scaling of the CO_2 and the CH_4 perturbations in this study are chosen so that the resulting ERFs are of similar magnitude. This allows an optimal comparison of the climate sensitivity parameters as these can depend on the magnitude of the perturbation (e.g., Hansen et al., 2005; Dietmüller et al., 2014). Our results suggest an efficacy of unity for the CH_4 perturbation when the climate sensitivity parameters are based on ERF. The climate sensitivity parameters based on SARF differ significantly between the CO_2 and the CH_4 increase, because of the large effect of chemical adjustments for the CH_4 perturbation. Thereby, our results support the finding that the climate sensitivity is in general less dependent on the type of perturbation for the ERF framework (e.g., Richardson et al., 2019). The multi-model mean efficacy based on ERF using the fixed SST method for a $3\times CH_4$ perturbation analyzed by Richardson et al. (2019) is slightly less than 1, with a spread of individual models of 0.56–1.15. In their study, the efficacy based on SARF is slightly less than 1 as well. In our study, the efficacy based on SARF is significantly larger than 1, i.e. about 3.6, because of the effect of chemical adjustments, which is not included in the estimate of Richardson et al. (2019).

The feedbacks corresponding to tropospheric O_3 changes in the full response are negative in contrast to previous estimates derived with the EMAC model with prescribed CH_4 mixing ratios at the lower boundary (Dietmüller et al., 2014; Stecher et al., 2021). As mentioned above, the explicit reduction of CH_4 mixing ratios allows for secondary feedbacks on O_3 to evolve and leads, more precisely, to reduced O_3 formation, which is also reflected by the negative radiative feedback. Furthermore, the feedback parameter of tropospheric O_3 derived from the multi-model mean analyzed by Stevenson et al. (2006) does not account for the CH_4 chemistry-climate feedback. The corresponding feedback parameter has been estimated at -0.007 ± 0.009 W m^{-2} K^{-1} by Heinze et al. (2019).

The reduction of CH_4 mixing ratios in the climate response induces a negative feedback parameter, which is estimated at -0.025 W m^{-2} K^{-1} for the CO_2 perturbation, and at -0.019 W m^{-2} K^{-1} for the CH_4 perturbation using the default radiative transfer scheme of EMAC. However, it is known that this radiative transfer scheme underestimates the direct radiative effect of CH_4 (Winterstein et al., 2019; Nützel et al., 2024). Therefore, we derive the radiative feedback also with the PSrad radiation scheme (Pincus and Stevens, 2013; Nützel et al., 2024), which suggests a clearly more pronounced feedback parameters of -0.041 W m^{-2} K^{-1} for the CO_2 perturbation, and of -0.089 W m^{-2} K^{-1} for the CH_4 perturbation. The PSrad feedback parameters are in the range of previous individual model estimates derived from CH_4 lifetime changes (Dietmüller et al., 2014; Heinze et al., 2019; Thornhill et al., 2021a).

Further, the default radiation scheme used in EMAC so far does not account for absorption of CH_4 in the solar SW spectrum. Recent studies have shown that accounting for SW absorption by CH_4 influences adjustment and feedback processes of, e.g. clouds (Smith et al., 2018; Modak et al., 2018; Allen et al., 2023, 2024). For an improved representation of the radiative effect of CH_4 in future studies, the PSrad radiation scheme (Pincus and Stevens, 2013) is now available for use in online EMAC simulations (Nützel et al., 2024).

This study focuses on the role of CH_4 for interactions between the gas-phase chemistry and climate change. However, further processes can also play a role, which are not accounted for by the used simulation set-up. For instance, chemistry-aerosol-cloud

coupling was identified to contribute to the ERF of CH_4 perturbations (Kurtén et al., 2011; O'Connor et al., 2022) and might therefore also influence the corresponding climate response. In addition, natural emission sources of CH_4, e.g. from wetlands or permafrost, have the potential to increase in a warming climate (e.g., O'Connor et al., 2010; Dean et al., 2018). For instance, the results of Thornhill et al. (2021a) suggest that the negative radiative effect corresponding to the shortening of the CH_4 lifetime is offset by the positive radiative effect of CH_4 emission increases from wetlands in response to a $4\times CO_2$ perturbation. The net effect of feedbacks on the gas-phase chemistry and on natural emissions influences the effect of associated secondary feedbacks, e.g. regarding the formation of O_3.

To conclude, the atmospheric abundance CH_4, and therefore its potential as a greenhouse gas, is linked to a number of complex interactions. This makes the assessment of the climate feedback of CH_4 and its indirect effects a non trivial undertaking, which requires comprehensive chemistry-climate simulations. The novelty of this study is that the feedback on CH_4 mixing ratios to changes of its chemical sink, and thereby also associated secondary feedbacks on OH and O_3, are accounted for explicitly, which is recommended to be adopted for further studies on chemical feedbacks.

Code and data availability. The Modular Earth Submodel System (MESSy; doi: 10.5281/zenodo.8360186) is continuously further developed and applied by a consortium of institutions. The usage of MESSy and access to the source code is licenced to all affiliates of institutions which are members of the MESSy Consortium. Institutions can become a member of the MESSy Consortium by signing the MESSy Memorandum of Understanding. More information can be found on the MESSy Consortium Website (http://www.messy-interface.org). The simulation results presented here are based on MESSy version 2.55.2 (The MESSy Consortium, 2021). Furthermore the exact code version used to produce the simulation results is archived at the German Climate Computing Center (DKRZ) and can be made available to members of the MESSy community upon request. The simulation results are available at the DKRZ DOKU long term archive under https://www.wdc-climate.de/ui/entry?acronym=DKRZ_LTA_1132_ds00001 (Stecher et al., 2024). The HadISST data (Rayner et al., 2003) are available from www.metoffice.gov.uk/hadobs (last access 16 September 2024).

Author contributions. FW and MP developed the concept of the study. LS performed the model simulations, analyzed the data and created the figures with significant contributions regarding the interpretation and evaluation of the model results from all coauthors. LS prepared the original draft and all authors contributed to the writing and reviewing of the manuscript.

Competing interests. Some authors are members of the editorial board of ACP.

Acknowledgements. We thank Simone Dietmüller (DLR) for doing the internal review. We used Climate Data Operators (CDO; https://code.mpimet.mpg.de/projects/cdo/, last access: 12 July 2024; Schulzweida, 2023) and netCDF Operators (NCO; Zender, 2024) for data processing. Further, we used Python, especially the packages Xarray (Hoyer and Hamman, 2017) and Matplotlib (Hunter, 2007), for data analysis and

producing the figures. We furthermore thank all contributors of the project ESCiMo (Earth System Chemistry integrated Modelling), which provides the model configuration and initial conditions. This work used resources of the Deutsches Klimarechenzentrum (DKRZ) granted by its Scientific Steering Committee (WLA) under project MIMETIC (bd1132).

Financial support. We acknowledge the financial support by the DFG Project IRFAM-ClimS (Vorhaben WI 5369/1-1) and the DLR internal project MABAK (Innovative Methoden zur Analyse und Bewertung von Veränderungen der Atmosphäre und des Klimasystems).

References

Abalos, M., Orbe, C., Kinnison, D. E., Plummer, D., Oman, L. D., Jöckel, P., Morgenstern, O., Garcia, R. R., Zeng, G., Stone, K. A., and Dameris, M.: Future trends in stratosphere-to-troposphere transport in CCMI models, Atmos. Chem. Phys., 20, 6883–6901, https://doi.org/10.5194/acp-20-6883-2020, 2020.

Allen, R. J., Zhao, X., Randles, C. A., Kramer, R. J., Samset, B. H., and Smith, C. J.: Surface warming and wetting due to methane's long-wave radiative effects muted by short-wave absorption, Nat. Geosci., https://doi.org/10.1038/s41561-023-01144-z, 2023.

Allen, R. J., Zhao, X., Randles, C. A., Kramer, R. J., Samset, B. H., and Smith, C. J.: Present-day methane shortwave absorption mutes surface warming relative to preindustrial conditions, Atmos. Chem. Phys., 24, 11207–11226, https://doi.org/10.5194/acp-24-11207-2024, 2024.

Ashmore, M. R.: Assessing the future global impacts of ozone on vegetation, Plant, Cell & Environment, 28, 949–964, https://doi.org/10.1111/j.1365-3040.2005.01341.x, 2005.

Butchart, N.: The Brewer-Dobson circulation, Reviews of Geophysics, 52, 157–184, https://doi.org/10.1002/2013RG000448, 2014.

Carpenter, L. J., Daniel, J., Fleming, E., Hanaoka, T., Hu, J., Ravishankara, A. R., Ross, M. N., Tilmes, S., Wallington, T. J., and Wuebbles, D. J.: Scenarios and information for policymakers, Chapter 6 in Scientific Assessment of Ozone Depletion: 2018, Global Ozone Research and Monitoring Project–Report No. 58, World Meteorological Organization, Geneva, Switzerland, 2018.

Chiodo, G., Polvani, L. M., Marsh, D. R., Stenke, A., Ball, W., Rozanov, E., Muthers, S., and Tsigaridis, K.: The Response of the Ozone Layer to Quadrupled CO_2 Concentrations, J. Climate, 31, 3893–3907, https://doi.org/10.1175/JCLI-D-17-0492.1, 2018.

Collins, W. J., Lamarque, J.-F., Schulz, M., Boucher, O., Eyring, V., Hegglin, M. I., Maycock, A., Myhre, G., Prather, M., Shindell, D., and Smith, S. J.: AerChemMIP: quantifying the effects of chemistry and aerosols in CMIP6, Geosci. Model Dev., 10, 585–607, https://doi.org/10.5194/gmd-10-585-2017, 2017.

Collins, W. J., Webber, C. P., Cox, P. M., Huntingford, C., Lowe, J., Sitch, S., Chadburn, S. E., Comyn-Platt, E., Harper, A. B., Hayman, G., and Powell, T.: Increased importance of methane reduction for a 1.5 degree target, Environ. Res. Lett., 13, 054003, https://doi.org/10.1088/1748-9326/aab89c, 2018.

Curry, C. L.: Modeling the soil consumption of atmospheric methane at the global scale, Global Biogeochem. Cy., 21, https://doi.org/10.1029/2006GB002818, 2007.

Dean, J. F., Middelburg, J. J., Röckmann, T., Aerts, R., Blauw, L. G., Egger, M., Jetten, M. S. M., de Jong, A. E. E., Meisel, O. H., Rasigraf, O., Slomp, C. P., in't Zandt, M. H., and Dolman, A. J.: Methane Feedbacks to the Global Climate System in a Warmer World, Rev. Geophys., 56, 207–250, https://doi.org/10.1002/2017RG000559, 2018.

Diehl, T., Heil, A., Chin, M., Pan, X., Streets, D., Schultz, M., and Kinne, S.: Anthropogenic, biomass burning, and volcanic emissions of black carbon, organic carbon, and SO_2 from 1980 to 2010 for hindcast model experiments, Atmos. Chem. Phys. Discuss., 12, 24895–24954, https://doi.org/10.5194/acpd-12-24895-2012, 2012.

Dietmüller, S., Ponater, M., and Sausen, R.: Interactive ozone induces a negative feedback in CO_2-driven climate change simulations, J. Geophys. Res. Atmos., 119, 1796–1805, https://doi.org/10.1002/2013JD020575, 2014.

Dietmüller, S., Jöckel, P., Tost, H., Kunze, M., Gellhorn, C., Brinkop, S., Frömming, C., Ponater, M., Steil, B., Lauer, A., and Hendricks, J.: A new radiation infrastructure for the Modular Earth Submodel System (MESSy, based on version 2.51), Geosci. Model Dev., 9, 2209–2222, https://doi.org/10.5194/gmd-9-2209-2016, 2016.

Etminan, M., Myhre, G., Highwood, E. J., and Shine, K. P.: Radiative forcing of carbon dioxide, methane, and nitrous oxide: A significant revision of the methane radiative forcing, Geophys. Res. Lett., 43, 12,614–12,623, https://doi.org/10.1002/2016GL071930, 2016.

800 Eyring, V., Bony, S., Meehl, G. A., Senior, C. A., Stevens, B., Stouffer, R. J., and Taylor, K. E.: Overview of the Coupled Model Intercomparison Project Phase 6 (CMIP6) experimental design and organization, Geosci. Model Dev., 9, 1937–1958, https://doi.org/10.5194/gmd-9-1937-2016, 2016.

Finney, D. L., Doherty, R. M., Wild, O., Young, P. J., and Butler, A.: Response of lightning NO_x emissions and ozone production to climate change: Insights from the Atmospheric Chemistry and Climate Model Intercomparison Project, Geophys. Res. Lett., 43, 5492–5500,

805   https://doi.org/10.1002/2016GL068825, 2016.

Finney, D. L., Doherty, R. M., Wild, O., Stevenson, D. S., MacKenzie, I. A., and Blyth, A. M.: A projected decrease in lightning under climate change, Nature Climate Change, 8, 210–213, https://doi.org/10.1038/s41558-018-0072-6, 2018.

Fiore, A. M., Dentener, F. J., Wild, O., Cuvelier, C., Schultz, M. G., Hess, P., Textor, C., Schulz, M., Doherty, R. M., Horowitz, L. W., MacKenzie, I. A., Sanderson, M. G., Shindell, D. T., Stevenson, D. S., Szopa, S., Van Dingenen, R., Zeng, G., Atherton, C., Bergmann,

810   D., Bey, I., Carmichael, G., Collins, W. J., Duncan, B. N., Faluvegi, G., Folberth, G., Gauss, M., Gong, S., Hauglustaine, D., Holloway, T., Isaksen, I. S. A., Jacob, D. J., Jonson, J. E., Kaminski, J. W., Keating, T. J., Lupu, A., Marmer, E., Montanaro, V., Park, R. J., Pitari, G., Pringle, K. J., Pyle, J. A., Schroeder, S., Vivanco, M. G., Wind, P., Wojcik, G., Wu, S., and Zuber, A.: Multimodel estimates of intercontinental source-receptor relationships for ozone pollution, J. Geophys. Res. Atmos., 114, https://doi.org/10.1029/2008JD010816, 2009.

815 Folberth, G. A., Staniaszek, Z., Archibald, A. T., Gedney, N., Griffiths, P. T., Jones, C. D., O'Connor, F. M., Parker, R. J., Sellar, A. A., and Wiltshire, A.: Description and Evaluation of an Emission-Driven and Fully Coupled Methane Cycle in UKESM1, J. Adv. Model. Earth Syst., 14, e2021MS002 982, https://doi.org/10.1029/2021MS002982, 2022.

Forster, P., Storelvmo, T., Armour, K., Collins, W., Dufresne, J.-L., Frame, D., Lunt, D., Mauritsen, T., Palmer, M., Watanabe, M., Wild, M., , and Zhang, H.: The Earth's Energy Budget, Climate Feedbacks, and Climate Sensitivity. Climate Change 2021: The Physical Science

820   Basis. Contribution of Working Group I to the Sixth Assessment Report of the Intergovernmental Panel on Climate Change [Masson-Delmotte, V., P. Zhai, A. Pirani, S.L. Connors, C. Péan, S. Berger, N. Caud, Y. Chen, L. Goldfarb, M.I. Gomis, M. Huang, K. Leitzell, E. Lonnoy, J.B.R. Matthews, T.K. Maycock, T. Waterfield, O. Yelekçi, R. Yu, and B. Zhou (eds.)], pp. 423–552, Cambridge University Press, Cambridge, United Kingdom and New York, NY, USA, https://doi.org/10.1017/9781009157896.009, 2021.

Forster, P. M., Richardson, T., Maycock, A. C., Smith, C. J., Samset, B. H., Myhre, G., Andrews, T., Pincus, R., and Schulz, M.: Recom-

825   mendations for diagnosing effective radiative forcing from climate models for CMIP6, J. Geophys. Res. Atmos, 121, 12,460–12,475, https://doi.org/10.1002/2016JD025320, 2016.

Frank, F.: Atmospheric methane and its isotopic composition in a changing climate: A modeling study, Ph.D. thesis, Ludwig-Maximilians-Universität München, https://doi.org/10.5282/edoc.22578, 2018.

Garny, H., Dameris, M., Randel, W., Bodeker, G. E., and Deckert, R.: Dynamically Forced Increase of Tropical Upwelling in the Lower

830   Stratosphere, Journal of the Atmospheric Sciences, 68, 1214–1233, https://doi.org/10.1175/2011JAS3701.1, 2011.

Giorgetta, M. A. and Bengtsson, L.: Potential role of the quasi-biennial oscillation in the stratosphere-troposphere exchange as found in water vapor in general circulation model experiments, J. Geophys. Res. Atmos., 104, 6003–6019, https://doi.org/10.1029/1998JD200112, 1999.

Granier, C., Bessagnet, B., Bond, T., D'Angiola, A., Denier van der Gon, H., Frost, G. J., Heil, A., Kaiser, J. W., Kinne, S., Klimont, Z., Kloster, S., Lamarque, J.-F., Liousse, C., Masui, T., Meleux, F., Mieville, A., Ohara, T., Raut, J.-C., Riahi, K., Schultz, M. G., Smith, S. J.,

835   Thompson, A., van Aardenne, J., van der Werf, G. R., and van Vuuren, D. P.: Evolution of anthropogenic and biomass burning emissions of air pollutants at global and regional scales during the 1980–2010 period, Climatic Change, 109, https://doi.org/10.1007/s10584-011-0154-1, 2011.

Grewe, V., Brunner, D., Dameris, M., Grenfell, J., Hein, R., Shindell, D., and Staehelin, J.: Origin and variability of upper tropospheric nitrogen oxides and ozone at northern mid-latitudes, Atmospheric Environment, 35, 3421–3433, https://doi.org/10.1016/S1352-840   2310(01)00134-0, 2001.

Grewe, V., Tsati, E., Mertens, M., Frömming, C., and Jöckel, P.: Contribution of emissions to concentrations: the TAGGING 1.0 submodel based on the Modular Earth Submodel System (MESSy 2.52), Geosci. Model Dev., 10, 2615–2633, https://doi.org/10.5194/gmd-10-2615-2017, 2017.

Griffiths, P. T., Murray, L. T., Zeng, G., Shin, Y. M., Abraham, N. L., Archibald, A. T., Deushi, M., Emmons, L. K., Galbally, I. E., Hassler, B., 845   Horowitz, L. W., Keeble, J., Liu, J., Moeini, O., Naik, V., O'Connor, F. M., Oshima, N., Tarasick, D., Tilmes, S., Turnock, S. T., Wild, O., Young, P. J., and Zanis, P.: Tropospheric ozone in CMIP6 simulations, Atmos. Chem. Phys., 21, 4187–4218, https://doi.org/10.5194/acp-21-4187-2021, 2021.

Hansen, J., Sato, M., Ruedy, R., Nazarenko, L., Lacis, A., Schmidt, G. A., Russell, G., Aleinov, I., Bauer, M., Bauer, S., Bell, N., Cairns, B., Canuto, V., Chandler, M., Cheng, Y., Del Genio, A., Faluvegi, G., Fleming, E., Friend, A., Hall, T., Jackman, C., Kelley, M., Kiang, 850   N., Koch, D., Lean, J., Lerner, J., Lo, K., Menon, S., Miller, R., Minnis, P., Novakov, T., Oinas, V., Perlwitz, J., Perlwitz, J., Rind, D., Romanou, A., Shindell, D., Stone, P., Sun, S., Tausnev, N., Thresher, D., Wielicki, B., Wong, T., Yao, M., and Zhang, S.: Efficacy of climate forcings, J. Geophys. Res. Atmos., 110, https://doi.org/10.1029/2005JD005776, 2005.

He, J., Naik, V., Horowitz, L. W., Dlugokencky, E., and Thoning, K.: Investigation of the global methane budget over 1980–2017 using GFDL-AM4.1, Atmos. Chem. Phys., 20, 805–827, https://doi.org/10.5194/acp-20-805-2020, 2020.

855   Heimann, I., Griffiths, P. T., Warwick, N. J., Abraham, N. L., Archibald, A. T., and Pyle, J. A.: Methane Emissions in a Chemistry-Climate Model: Feedbacks and Climate Response, J. Adv. Model. Earth Syst., 12, e2019MS002 019, https://doi.org/10.1029/2019MS002019, 2020.

Heinze, C., Eyring, V., Friedlingstein, P., Jones, C., Balkanski, Y., Collins, W., Fichefet, T., Gao, S., Hall, A., Ivanova, D., Knorr, W., Knutti, R., Löw, A., Ponater, M., Schultz, M. G., Schulz, M., Siebesma, P., Teixeira, J., Tselioudis, G., and Vancoppenolle, M.: ESD Reviews: 860   Climate feedbacks in the Earth system and prospects for their evaluation, Earth Syst. Dynam., 10, 379–452, https://doi.org/10.5194/esd-10-379-2019, 2019.

Holmes, C. D.: Methane Feedback on Atmospheric Chemistry: Methods, Models, and Mechanisms, J. Adv. Model. Earth Syst., 10, 1087–1099, https://doi.org/10.1002/2017MS001196, 2018.

Hoyer, S. and Hamman, J.: xarray: N-D labeled arrays and datasets in Python, Journal of Open Research Software, 5, 865   https://doi.org/10.5334/jors.148, 2017.

Hunter, J. D.: Matplotlib: A 2D graphics environment, Comput Sci Eng, 9, 90–95, https://doi.org/10.1109/MCSE.2007.55, 2007.

IPCC: Climate Change 2021: The Physical Science Basis. Contribution of Working Group I to the Sixth Assessment Report of the Intergovernmental Panel on Climate Change [Masson-Delmotte, V., P. Zhai, A. Pirani, S.L. Connors, C. Péan, S. Berger, N. Caud, Y. Chen, L. Goldfarb, M.I. Gomis, M. Huang, K. Leitzell, E. Lonnoy, J.B.R. Matthews, T.K. Maycock, T. Waterfield, O. Yelekçi, R. Yu, and B. Zhou 870   (eds.)], Cambridge University Press, Cambridge, United Kingdom and New York, NY, USA, https://doi.org/10.1017/9781009157896, 2021.

Jöckel, P., Tost, H., Pozzer, A., Kunze, M., Kirner, O., Brenninkmeijer, C. A. M., Brinkop, S., Cai, D. S., Dyroff, C., Eckstein, J., Frank, F., Garny, H., Gottschaldt, K.-D., Graf, P., Grewe, V., Kerkweg, A., Kern, B., Matthes, S., Mertens, M., Meul, S., Neumaier, M., Nützel, M., Oberländer-Hayn, S., Ruhnke, R., Runde, T., Sander, R., Scharffe, D., and Zahn, A.: Earth System Chemistry integrated Mod-

875 elling (ESCiMo) with the Modular Earth Submodel System (MESSy) version 2.51, Geoscientific Model Development, 9, 1153–1200, https://doi.org/10.5194/gmd-9-1153-2016, 2016.

Kerkweg, A., Buchholz, J., Ganzeveld, L., Pozzer, A., Tost, H., and Jöckel, P.: Technical Note: An implementation of the dry removal processes DRY DEPosition and SEDImentation in the Modular Earth Submodel System (MESSy), Atmos. Chem. Phys., 6, 4617–4632, https://doi.org/10.5194/acp-6-4617-2006, 2006a.

880 Kerkweg, A., Sander, R., Tost, H., and Jöckel, P.: Technical note: Implementation of prescribed (OFFLEM), calculated (ONLEM), and pseudo-emissions (TNUDGE) of chemical species in the Modular Earth Submodel System (MESSy), Atmos. Chem. Phys., 6, 3603–3609, https://doi.org/10.5194/acp-6-3603-2006, 2006b.

Kunze, M., Godolt, M., Langematz, U., Grenfell, J., Hamann-Reinus, A., and Rauer, H.: Investigating the early Earth faint young Sun problem with a general circulation model, Planet. Space Sci., 98, 77–92, https://doi.org/10.1016/j.pss.2013.09.011, planetary evolution
885 and life, 2014.

Kurtén, T., Zhou, L., Makkonen, R., Merikanto, J., Räisänen, P., Boy, M., Richards, N., Rap, A., Smolander, S., Sogachev, A., Guenther, A., Mann, G. W., Carslaw, K., and Kulmala, M.: Large methane releases lead to strong aerosol forcing and reduced cloudiness, Atmos. Chem. and Phys., 11, 6961–6969, https://doi.org/10.5194/acp-11-6961-2011, 2011.

Lamarque, J.-F., Bond, T. C., Eyring, V., Granier, C., Heil, A., Klimont, Z., Lee, D., Liousse, C., Mieville, A., Owen, B., Schultz, M. G.,
890 Shindell, D., Smith, S. J., Stehfest, E., Van Aardenne, J., Cooper, O. R., Kainuma, M., Mahowald, N., McConnell, J. R., Naik, V., Riahi, K., and van Vuuren, D. P.: Historical (1850–2000) gridded anthropogenic and biomass burning emissions of reactive gases and aerosols: methodology and application, Atmos. Chem. Phys., 10, 7017–7039, https://doi.org/10.5194/acp-10-7017-2010, 2010.

Lan, X., Thoning, K., and Dlugokencky, E.: Trends in globally-averaged CH_4, N_2O, and SF_6 determined from NOAA Global Monitoring Laboratory measurements, https://doi.org/10.15138/P8XG-AA10, 2023.

895 Lawrence, M. G., Jöckel, and von Kuhlmann, R.: What does the global mean OH concentration tell us?, Atmos. Chem. Phys., 1, 37–49, https://doi.org/10.5194/acp-1-37-2001, 2001.

Li, F. and Newman, P.: Prescribing stratospheric chemistry overestimates southern hemisphere climate change during austral spring in response to quadrupled CO_2, Clim. Dyn., 61, 1105—-1122, https://doi.org/10.1007/s00382-022-06588-4, 2023.

Liang, Q., Stolarski, R. S., Kawa, S. R., Nielsen, J. E., Douglass, A. R., Rodriguez, J. M., Blake, D. R., Atlas, E. L., and Ott, L. E.: Finding
900 the missing stratospheric Br_y: a global modeling study of $CHBr_3$ and CH_2Br_2, Atmospheric Chemistry and Physics, 10, 2269–2286, https://doi.org/10.5194/acp-10-2269-2010, 2010.

Marsh, D. R., Lamarque, J.-F., Conley, A. J., and Polvani, L. M.: Stratospheric ozone chemistry feedbacks are not critical for the determination of climate sensitivity in CESM1(WACCM), Geophys. Res. Lett., 43, 3928–3934, https://doi.org/10.1002/2016GL068344, 2016.

Meinshausen, M., Smith, S. J., Calvin, K., Daniel, J. S., Kainuma, M. L. T., Lamarque, J.-F., Matsumoto, K., Montzka, S. A., Raper, S. C. B.,
905 Riahi, K., Thomson, A., Velders, G. J. M., and van Vuuren, D. P.: The RCP greenhouse gas concentrations and their extensions from 1765 to 2300, Climatic Change, 109, 1573–1480, https://doi.org/10.1007/s10584-011-0156-z, 2011.

Meinshausen, M., Vogel, E., Nauels, A., Lorbacher, K., Meinshausen, N., Etheridge, D. M., Fraser, P. J., Montzka, S. A., Rayner, P. J., Trudinger, C. M., Krummel, P. B., Beyerle, U., Canadell, J. G., Daniel, J. S., Enting, I. G., Law, R. M., Lunder, C. R., O'Doherty, S., Prinn, R. G., Reimann, S., Rubino, M., Velders, G. J. M., Vollmer, M. K., Wang, R. H. J., and Weiss, R.: Historical greenhouse gas
910 concentrations for climate modelling (CMIP6), Geosci. Model Dev, 10, 2057–2116, https://doi.org/10.5194/gmd-10-2057-2017, 2017.

Modak, A., Bala, G., Caldeira, K., and Cao, L.: Does shortwave absorption by methane influence its effectiveness?, Climate Dyn., 51, 3653–3672, https://doi.org/10.1007/s00382-018-4102-x, 2018.

Nowack, P. J., Luke Abraham, N., Maycock, A. C., Braesicke, P., Gregory, J. M., Joshi, M. M., Osprey, A., and Pyle, J. A.: A large ozone-circulation feedback and its implications for global warming assessments, Nature Climate Change, 5, 41–45, https://doi.org/10.1038/nclimate2451, 2015.

Nowack, P. J., Abraham, N. L., Braesicke, P., and Pyle, J. A.: The Impact of Stratospheric Ozone Feedbacks on Climate Sensitivity Estimates, J. Geophys. Res. Atmos., 123, 4630–4641, https://doi.org/10.1002/2017JD027943, 2018.

Nützel, M., Stecher, L., Jöckel, P., Winterstein, F., Dameris, M., Ponater, M., Graf, P., and Kunze, M.: Updating the radiation infrastructure in MESSy (based on MESSy version 2.55), Geosci. Model Dev., 17, 5821–5849, https://doi.org/10.5194/gmd-17-5821-2024, 2024.

Nuvolone, D., Petri, D., and Voller, F.: The effects of ozone on human health, Environ. Sci. Pollut. Res., 25, 8074–8088, https://doi.org/10.1007/s11356-017-9239-3, 2018.

Ocko, I. B., Sun, T., Shindell, D., Oppenheimer, M., Hristov, A. N., Pacala, S. W., Mauzerall, D. L., Xu, Y., and Hamburg, S. P.: Acting rapidly to deploy readily available methane mitigation measures by sector can immediately slow global warming, Environ. Res. Lett., 16, 054 042, https://doi.org/10.1088/1748-9326/abf9c8, 2021.

O'Connor, F. M., Boucher, O., Gedney, N., Jones, C. D., Folberth, G. A., Coppell, R., Friedlingstein, P., Collins, W. J., Chappellaz, J., Ridley, J., and Johnson, C. E.: Possible role of wetlands, permafrost, and methane hydrates in the methane cycle under future climate change: A review, Rev. Geophys., 48, https://doi.org/10.1029/2010RG000326, 2010.

O'Connor, F. M., Johnson, B. T., Jamil, O., Andrews, T., Mulcahy, J. P., and Manners, J.: Apportionment of the Pre-Industrial to Present-Day Climate Forcing by Methane Using UKESM1: The Role of the Cloud Radiative Effect, J. Adv. Model. Earth Syst., 14, e2022MS002 991, https://doi.org/10.1029/2022MS002991, 2022.

Pincus, R. and Stevens, B.: Paths to accuracy for radiation parameterizations in atmospheric models, J. Adv. Model. Earth Syst., 5, 225–233, https://doi.org/10.1002/jame.20027, 2013.

Portmann, R. W. and Solomon, S.: Indirect radiative forcing of the ozone layer during the 21st century, Geophys. Res. Lett., 34, https://doi.org/10.1029/2006GL028252, 2007.

Pozzer, A., Jöckel, P., Sander, R., Williams, J., Ganzeveld, L., and Lelieveld, J.: Technical Note: The MESSy-submodel AIRSEA calculating the air-sea exchange of chemical species, Atmos. Chem. Phys., 6, 5435–5444, https://doi.org/10.5194/acp-6-5435-2006, 2006.

Prather, M. J., Holmes, C. D., and Hsu, J.: Reactive greenhouse gas scenarios: Systematic exploration of uncertainties and the role of atmospheric chemistry, Geophys. Res. Lett., 39, https://doi.org/10.1029/2012GL051440, 2012.

Ramaswamy, V., Collins, W., Haywood, J., Lean, J., Mahowald, N., Myhre, G., Naik, V., Shine, K. P., Soden, B., Stenchikov, G., and Storelvmo, T.: Radiative Forcing of Climate: The Historical Evolution of the Radiative Forcing Concept, the Forcing Agents and their Quantification, and Applications, Meteorological Monographs, 59, 14.1 – 14.101, https://doi.org/10.1175/AMSMONOGRAPHS-D-19-0001.1, 2018.

Rayner, N. A., Parker, D. E., Horton, E. B., Folland, C. K., Alexander, L. V., Rowell, D. P., Kent, E. C., and Kaplan, A.: Global analyses of sea surface temperature, sea ice, and night marine air temperature since the late nineteenth century, J. Geophys. Res. Atmos., 108, 4407, https://doi.org/10.1029/2002JD002670, 2003.

Richardson, T. B., Forster, P. M., Smith, C. J., Maycock, A. C., Wood, T., Andrews, T., Boucher, O., Faluvegi, G., Fläschner, D., Hodnebrog, Ø., Kasoar, M., Kirkevåg, A., Lamarque, J.-F., Mülmenstädt, J., Myhre, G., Olivié, D., Portmann, R. W., Samset, B. H., Shawki, D., Shindell, D., Stier, P., Takemura, T., Voulgarakis, A., and Watson-Parris, D.: Efficacy of Climate Forcings in PDRMIP Models, J. Geophys. Res. Atmos., 124, 12 824–12 844, https://doi.org/10.1029/2019JD030581, 2019.

950 Rieger, V. S., Mertens, M., and Grewe, V.: An advanced method of contributing emissions to short-lived chemical species (OH and HO$_2$): the TAGGING 1.1 submodel based on the Modular Earth Submodel System (MESSy 2.53), Geosci. Model Dev., 11, 2049–2066, https://doi.org/10.5194/gmd-11-2049-2018, 2018.

Rind, D., Shindell, D., Lonergan, P., and Balachandran, N. K.: Climate Change and the Middle Atmosphere. Part III: The Doubled CO2 Climate Revisited, Journal of Climate, 11, 876 – 894, https://doi.org/10.1175/1520-0442(1998)011<0876:CCATMA>2.0.CO;2, 1998.

955 Roeckner, E., Siebert, T., and Feichter, J.: Climatic response to anthropogenic sulfate forcing simulated with a general circulation model, Aerosol Forcing of Climate, pp. 349–362, 1995.

Roeckner, E., Bäuml, G., Bonaventura, L., Brokopf, R., Esch, M., Giorgetta, M., Hagemann, S., Kirchner, I., Kornblueh, L., Manzini, E., Rhodin, A., Schlese, U., Schulzweida, U., and Tompkins, A.: The atmospheric general circulation model ECHAM5. PART I: Model description, Report / Max-Planck-Institut für Meteorologie, 349, https://hdl.handle.net/11858/00-001M-0000-0012-0144-5, 2003.

960 Rosenfield, J. E., Douglass, A. R., and Considine, D. B.: The impact of increasing carbon dioxide on ozone recovery, J. Geophys. Res. Atmos., 107, ACH 7–1–ACH 7–9, https://doi.org/10.1029/2001JD000824, 2002.

Sand, M., Skeie, R. B., Sandstad, M., Krishnan, S., Myhre, G., Bryant, H., Derwent, R., Hauglustaine, D., Paulot, F., Prather, M., and Stevenson, D.: A multi-model assessment of the Global Warming Potential of hydrogen, Communications Earth Environment, 4, https://doi.org/10.1038/s43247-023-00857-8, 2023.

965 Sander, R., Jöckel, P., Kirner, O., Kunert, A. T., Landgraf, J., and Pozzer, A.: The photolysis module JVAL-14, compatible with the MESSy standard, and the JVal PreProcessor (JVPP), Geosci. Model Dev., 7, 2653–2662, https://doi.org/10.5194/gmd-7-2653-2014, 2014.

Sander, R., Baumgaertner, A., Cabrera-Perez, D., Frank, F., Gromov, S., Grooß, J.-U., Harder, H., Huijnen, V., Jöckel, P., Karydis, V. A., Niemeyer, K. E., Pozzer, A., Riede, H., Schultz, M. G., Taraborrelli, D., and Tauer, S.: The community atmospheric chemistry box model CAABA/MECCA-4.0, Geosci. Model Dev., 12, 1365–1385, https://doi.org/10.5194/gmd-12-1365-2019, 2019.

970 Saunois, M., Jackson, R. B., Bousquet, P., Poulter, B., and Canadell, J. G.: The growing role of methane in anthropogenic climate change, Environ. Res. Lett., 11, 120 207, https://doi.org/10.1088/1748-9326/11/12/120207, 2016.

Saunois, M., Stavert, A. R., Poulter, B., Bousquet, P., Canadell, J. G., Jackson, R. B., Raymond, P. A., Dlugokencky, E. J., Houweling, S., Patra, P. K., Ciais, P., Arora, V. K., Bastviken, D., Bergamaschi, P., Blake, D. R., Brailsford, G., Bruhwiler, L., Carlson, K. M., Carrol, M., Castaldi, S., Chandra, N., Crevoisier, C., Crill, P. M., Covey, K., Curry, C. L., Etiope, G., Frankenberg, C., Gedney, N., Hegglin, M. I.,

975 Höglund-Isaksson, L., Hugelius, G., Ishizawa, M., Ito, A., Janssens-Maenhout, G., Jensen, K. M., Joos, F., Kleinen, T., Krummel, P. B., Langenfelds, R. L., Laruelle, G. G., Liu, L., Machida, T., Maksyutov, S., McDonald, K. C., McNorton, J., Miller, P. A., Melton, J. R., Morino, I., Müller, J., Murguia-Flores, F., Naik, V., Niwa, Y., Noce, S., O'Doherty, S., Parker, R. J., Peng, C., Peng, S., Peters, G. P., Prigent, C., Prinn, R., Ramonet, M., Regnier, P., Riley, W. J., Rosentreter, J. A., Segers, A., Simpson, I. J., Shi, H., Smith, S. J., Steele, L. P., Thornton, B. F., Tian, H., Tohjima, Y., Tubiello, F. N., Tsuruta, A., Viovy, N., Voulgarakis, A., Weber, T. S., van Weele, M., van der

980 Werf, G. R., Weiss, R. F., Worthy, D., Wunch, D., Yin, Y., Yoshida, Y., Zhang, W., Zhang, Z., Zhao, Y., Zheng, B., Zhu, Q., Zhu, Q., and Zhuang, Q.: The Global Methane Budget 2000–2017, Earth Syst. Sci. Data, 12, 1561–1623, https://doi.org/10.5194/essd-12-1561-2020, 2020.

Schulzweida, U.: CDO User Guide (2.3.0), Zenodo, https://doi.org/10.5281/zenodo.10020800, 2023.

Shindell, D., Kuylenstierna, J. C. I., Vignati, E., van Dingenen, R., Amann, M., Klimont, Z., Anenberg, S. C., Muller, N., Janssens-Maenhout,

985 G., Raes, F., Schwartz, J., Faluvegi, G., Pozzoli, L., Kupiainen, K., Höglund-Isaksson, L., Emberson, L., Streets, D., Ramanathan, V., Hicks, K., Oanh, N. T. K., Milly, G., Williams, M., Demkine, V., and Fowler, D.: Simultaneously Mitigating Near-Term Climate Change and Improving Human Health and Food Security, Science, 335, 183–189, https://doi.org/10.1126/science.1210026, 2012.

Shindell, D. T., Faluvegi, G., Bell, N., and Schmidt, G. A.: An emissions-based view of climate forcing by methane and tropospheric ozone, Geophys. Res. Lett., 32, https://doi.org/10.1029/2004GL021900, 2005.

990 Shindell, D. T., Faluvegi, G., Koch, D. M., Schmidt, G. A., Unger, N., and Bauer, S. E.: Improved Attribution of Climate Forcing to Emissions, Science, 326, 716–718, https://doi.org/10.1126/science.1174760, 2009.

Shindell, D. T., Pechony, O., Voulgarakis, A., Faluvegi, G., Nazarenko, L., Lamarque, J.-F., Bowman, K., Milly, G., Kovari, B., Ruedy, R., and Schmidt, G. A.: Interactive ozone and methane chemistry in GISS-E2 historical and future climate simulations, Atmos. Chem. Phys., 13, 2653–2689, https://doi.org/10.5194/acp-13-2653-2013, 2013.

995 Shine, K. P., Cook, J., Highwood, E. J., and Joshi, M. M.: An alternative to radiative forcing for estimating the relative importance of climate change mechanisms, Geophys. Res. Lett., 30, https://doi.org/10.1029/2003GL018141, 2003.

Sitch, S., Cox, P. M., Collins, W. J., and Huntingford, C.: Indirect radiative forcing of climate change through ozone effects on the land-carbon sink, Nature, 448, 791–794, https://doi.org/10.1038/nature06059, 2007.

Smith, C. J., Kramer, R. J., Myhre, G., Forster, P. M., Soden, B., Andrews, T., Boucher, O., Faluvegi, G., Fläschner, D., Hodnebrog, Ø.,

1000 Kasoar, M., Kharin, V., Kirkevåg, A., Lamarque, J.-F., Mülmenstädt, J., Olivié, D., Richardson, T., Samset, B. H., Shindell, D., Stier, P., Takemura, T., Voulgarakis, A., and Watson-Parris, D.: Understanding Rapid Adjustments to Diverse Forcing Agents, Geophys. Res. Lett., 45, 12,023–12,031, https://doi.org/10.1029/2018GL079826, 2018.

Spahni, R., Wania, R., Neef, L., van Weele, M., Pison, I., Bousquet, P., Frankenberg, C., Foster, P. N., Joos, F., Prentice, I. C., and van Velthoven, P.: Constraining global methane emissions and uptake by ecosystems, Biogeosciences, 8, 1643–1665,

1005 https://doi.org/10.5194/bg-8-1643-2011, 2011.

Staniaszek, Z., Griffiths, P. T., Folberth, G. A., O'Connor, F. M., Abraham, N. L., and Archibald, A. T.: The role of future anthropogenic methane emissions in air quality and climate, npj Clim Atmos Sci, 5, https://doi.org/10.1038/s41612-022-00247-5, 2022.

Stecher, L.: The role of methane for chemistry-climate interactions, https://doi.org/10.5282/edoc.33812, 2024.

Stecher, L., Winterstein, F., Dameris, M., Jöckel, P., Ponater, M., and Kunze, M.: Slow feedbacks resulting from strongly enhanced

1010 atmospheric methane mixing ratios in a chemistry–climate model with mixed–layer ocean, Atmos. Chem. Phys., 21, 731–754, https://doi.org/10.5194/acp-21-731-2021, 2021.

Stecher, L., Winterstein, F., Jöckel, P., Ponater, M., Mertens, M., and Dameris, M.: EMAC simulations of project IRFAM-ClimS with ECHAM5 radiation and interactive chemistry, https://www.wdc-climate.de/ui/entry?acronym=DKRZ_LTA_1132_ds00001, 2024.

Stevenson, D. S., Dentener, F. J., Schultz, M. G., Ellingsen, K., van Noije, T. P. C., Wild, O., Zeng, G., Amann, M., Atherton, C. S., Bell, N.,

1015 Bergmann, D. J., Bey, I., Butler, T., Cofala, J., Collins, W. J., Derwent, R. G., Doherty, R. M., Drevet, J., Eskes, H. J., Fiore, A. M., Gauss, M., Hauglustaine, D. A., Horowitz, L. W., Isaksen, I. S. A., Krol, M. C., Lamarque, J.-F., Lawrence, M. G., Montanaro, V., Müller, J.-F., Pitari, G., Prather, M. J., Pyle, J. A., Rast, S., Rodriguez, J. M., Sanderson, M. G., Savage, N. H., Shindell, D. T., Strahan, S. E., Sudo, K., and Szopa, S.: Multimodel ensemble simulations of present-day and near-future tropospheric ozone, J. Geophys. Res. Atmos., 111, https://doi.org/10.1029/2005JD006338, 2006.

1020 Stevenson, D. S., Young, P. J., Naik, V., Lamarque, J.-F., Shindell, D. T., Voulgarakis, A., Skeie, R. B., Dalsoren, S. B., Myhre, G., Berntsen, T. K., Folberth, G. A., Rumbold, S. T., Collins, W. J., MacKenzie, I. A., Doherty, R. M., Zeng, G., van Noije, T. P. C., Strunk, A., Bergmann, D., Cameron-Smith, P., Plummer, D. A., Strode, S. A., Horowitz, L., Lee, Y. H., Szopa, S., Sudo, K., Nagashima, T., Josse, B., Cionni, I., Righi, M., Eyring, V., Conley, A., Bowman, K. W., Wild, O., and Archibald, A.: Tropospheric ozone changes, radiative forcing and attribution to emissions in the Atmospheric Chemistry and Climate Model Intercomparison Project (ACCMIP), Atmos. Chem. Phys.,

1025 13, 3063–3085, https://doi.org/10.5194/acp-13-3063-2013, 2013.

Stevenson, D. S., Zhao, A., Naik, V., O'Connor, F. M., Tilmes, S., Zeng, G., Murray, L. T., Collins, W. J., Griffiths, P. T., Shim, S., Horowitz, L. W., Sentman, L. T., and Emmons, L.: Trends in global tropospheric hydroxyl radical and methane lifetime since 1850 from AerChem-MIP, Atmos. Chem. Phys, 20, 12 905–12 920, https://doi.org/10.5194/acp-20-12905-2020, 2020.

Stuber, N., Sausen, R., and Ponater, M.: Stratosphere adjusted radiative forcing calculations in a comprehensive climate model, Theor. Appl. Climatol., 68, 125–135, https://doi.org/10.1007/s007040170041, 2001.

The MESSy Consortium: The Modular Earth Submodel System, Zenodo, https://doi.org/10.5281/zenodo.8360276, 2021.

Thornhill, G., Collins, W., Olivié, D., Skeie, R. B., Archibald, A., Bauer, S., Checa-Garcia, R., Fiedler, S., Folberth, G., Gjermundsen, A., Horowitz, L., Lamarque, J.-F., Michou, M., Mulcahy, J., Nabat, P., Naik, V., O'Connor, F. M., Paulot, F., Schulz, M., Scott, C. E., Séférian, R., Smith, C., Takemura, T., Tilmes, S., Tsigaridis, K., and Weber, J.: Climate-driven chemistry and aerosol feedbacks in CMIP6 Earth system models, Atmos. Chem. Phys., 21, 1105–1126, https://doi.org/10.5194/acp-21-1105-2021, 2021a.

Thornhill, G. D., Collins, W. J., Kramer, R. J., Olivié, D., Skeie, R. B., O'Connor, F. M., Abraham, N. L., Checa-Garcia, R., Bauer, S. E., Deushi, M., Emmons, L. K., Forster, P. M., Horowitz, L. W., Johnson, B., Keeble, J., Lamarque, J.-F., Michou, M., Mills, M. J., Mulcahy, J. P., Myhre, G., Nabat, P., Naik, V., Oshima, N., Schulz, M., Smith, C. J., Takemura, T., Tilmes, S., Wu, T., Zeng, G., and Zhang, J.: Effective radiative forcing from emissions of reactive gases and aerosols – a multi-model comparison, Atmos. Chem. Phys., 21, 853–874, https://doi.org/10.5194/acp-21-853-2021, 2021b.

Tost, H., Jöckel, P., and Lelieveld, J.: Lightning and convection parameterisations - uncertainties in global modelling, Atmos. Chem. Phys., 7, 4553–4568, https://doi.org/10.5194/acp-7-4553-2007, 2007.

Vella, R., Forrest, M., Lelieveld, J., and Tost, H.: Isoprene and monoterpene simulations using the chemistry–climate model EMAC (v2.55) with interactive vegetation from LPJ-GUESS (v4.0), Geosci. Model Dev., 16, 885–906, https://doi.org/10.5194/gmd-16-885-2023, 2023.

Voulgarakis, A., Naik, V., Lamarque, J.-F., Shindell, D. T., Young, P. J., Prather, M. J., Wild, O., Field, R. D., Bergmann, D., Cameron-Smith, P., Cionni, I., Collins, W. J., Dalsøren, S. B., Doherty, R. M., Eyring, V., Faluvegi, G., Folberth, G. A., Horowitz, L. W., Josse, B., MacKenzie, I. A., Nagashima, T., Plummer, D. A., Righi, M., Rumbold, S. T., Stevenson, D. S., Strode, S. A., Sudo, K., Szopa, S., and Zeng, G.: Analysis of present day and future OH and methane lifetime in the ACCMIP simulations, Atmos. Chem. Phys., 13, 2563–2587, https://doi.org/10.5194/acp-13-2563-2013, 2013.

Wang, H., Lu, X., Seco, R., Stavrakou, T., Karl, T., Jiang, X., Gu, L., and Guenther, A. B.: Modeling Isoprene Emission Response to Drought and Heatwaves Within MEGAN Using Evapotranspiration Data and by Coupling With the Community Land Model, J Adv Model Earth Sy, 14, e2022MS003 174, https://doi.org/10.1029/2022MS003174, e2022MS003174 2022MS003174, 2022.

Warwick, N. J., Pyle, J. A., Carver, G. D., Yang, X., Savage, N. H., O'Connor, F. M., and Cox, R. A.: Global modeling of biogenic bromocarbons, J. Geophys. Res. Atmos., 111, https://doi.org/https://doi.org/10.1029/2006JD007264, 2006.

Winterstein, F., Tanalski, F., Jöckel, P., Dameris, M., and Ponater, M.: Implication of strongly increased atmospheric methane concentrations for chemistry–climate connections, Atmos. Chem. Phys., 19, 7151–7163, https://doi.org/10.5194/acp-19-7151-2019, 2019.

WMO: WMO Greenhouse Gas Bulletin (GHG Bulletin) - No.18: The State of Greenhouse Gases in the Atmosphere Based on Global Observations through 2021, https://library.wmo.int/idurl/4/58743, 2022.

Zanis, P., Akritidis, D., Turnock, S., Naik, V., Szopa, S., Georgoulias, A. K., Bauer, S. E., Deushi, M., Horowitz, L. W., Keeble, J., Sager, P. L., O'Connor, F. M., Oshima, N., Tsigaridis, K., and van Noije, T.: Climate change penalty and benefit on surface ozone: a global perspective based on CMIP6 earth system models, Environ. Res. Lett., 17, 024 014, https://doi.org/10.1088/1748-9326/ac4a34, 2022.

Zender, C. S.: netCDF Operator (NCO) User Guide, http://nco.sf.net/nco.pdf, 2024.

Zhou, S. S., Tai, A. P. K., Sun, S., Sadiq, M., Heald, C. L., and Geddes, J. A.: Coupling between surface ozone and leaf area index in a chemical transport model: strength of feedback and implications for ozone air quality and vegetation health, Atmos. Chem. Phys., 18, 14 133–14 148, https://doi.org/10.5194/acp-18-14133-2018, 2018.

1065